

The Lagrangian hydrodynamics code MAGMA2

S. Rosswog^{*1}

¹ *The Oskar Klein Centre, Department of Astronomy, AlbaNova, Stockholm University, SE-106 91 Stockholm, Sweden*

Draft version

ABSTRACT

We present the methodology and performance of the new Lagrangian hydrodynamics code MAGMA2, a Smoothed Particle Hydrodynamics code that benefits from a number of non-standard enhancements. By default it uses high-order smoothing kernels and wherever gradients are needed, they are calculated via accurate matrix inversion techniques, but a more conventional formulation with kernel gradients has also been implemented for comparison purposes. We also explore a matrix inversion formulation of SPH with a symmetrisation in the particle indices that is not frequently used. We find interesting advantages of this formulation in some of the tests, for example, a substantial reduction of surface tension effects for non-ideal particle setups and more accurate peak densities in Sedov blast waves. MAGMA2 uses artificial viscosity, but enhanced by techniques that are commonly used in finite volume schemes such as reconstruction and slope limiting. While simple to implement, this approach efficiently suppresses particle noise, but at the same time drastically reduces dissipation in locations where it is not needed and actually unwanted. We demonstrate the performance of the new code in a number of challenging benchmark tests including e.g. multi-dimensional vorticity creating Schulz-Rinne-type Riemann problems and more astrophysical tests such as a collision between two stars to demonstrate its robustness and excellent conservation properties.

Key words: hydrodynamics – methods: numerical – instabilities – shock waves – software: simulations – transients: tidal disruption events

1 INTRODUCTION

A Lagrangian formulation of hydrodynamics is a natural choice for many astrophysical problems. Smoothed Particle Hydrodynamics (SPH) (Lucy 1977; Monaghan 1977) is the most wide-spread Lagrangian method in astrophysics. It is entirely mesh-free and the equations can be symmetrised in a way so that mass, energy, momentum and angular momentum are conserved by construction. As it is derived, SPH is entirely dissipationless and therefore needs to be augmented by additional measures to produce appropriate amounts of entropy in shocks. This is traditionally done via artificial viscosity, but also Riemann solver approaches have been explored (Inutsuka 2002; Cha & Whitworth 2003; Cha et al. 2010; Murante et al. 2011; Puri & Ramachandran 2014).

In SPH one calculates the density via a smooth weighting of nearby particle masses and this smooth density estimate enters the calculation of pressures that drive the motion. The internal energy, in contrast, is evolved via a straight-forward discretisation of the Lagrangian energy conservation law and does therefore not involve a smoothing process. This potentially different inherent smoothness of both quantities can lead to unintended “pressure blips” when setting up contact discontinuities. These blips cause surface tension effects that can suppress weakly triggered fluid instabilities (Agertz et al.

2007; McNally et al. 2012). Such effects can be counterbalanced by a careful setup of initial conditions with consistent smoothness, by alternative expressions for SPH volume elements (Ritchie & Thomas 2001; Saitoh & Makino 2013; Hopkins 2013; Rosswog 2015a; Cabezón et al. 2017) or by adding artificial conductivity terms to smooth out sharp transitions in the internal energy (Price 2008; Valdarnini 2012).

These issues have spurred further developments on Lagrangian hydrodynamics, many of which have employed techniques from finite volume Eulerian hydrodynamics. The *Arepo* code (Springel 2010a), for example, tessellates space into Voronoi cells and evolves the hydrodynamic equations via a Riemann solver-based finite volume strategy. Such finite volume approaches, however, are not bound to Voronoi or other meshes and can actually also be applied to hydrodynamic schemes which use particles. Several such finite volume particle schemes have been suggested in the applied mathematics literature (Ben Moussa et al. 1999; Vila 1999; Hietel et al. 2000; Junk 2003), but they have only recently found their way into astrophysics (Gaburov & Nitadori 2011; Hopkins 2015; Hubber et al. 2018) where they have delivered accurate results.

Also on the SPH-side there have been several new developments. Apart from the above mentioned volume element improvements, substantially more accurate gradient estimates have been implemented (García-Senz et al. 2012; Cabezón et al. 2012; Rosswog 2015a). The perhaps most advanced SPH scheme to date (Fron-

* E-mail: stephan.rosswog@astro.su.se

2 Rosswog

tiere et al. 2017) uses a reproducing kernel methodology (Liu et al. 1995) together with a sophisticated artificial dissipation scheme. They find good performance in a number of benchmark tests that are generally considered difficult for SPH. While the increasing cross-fertilisation between different methods has been very beneficial, the boundaries between different numerical schemes and their naming conventions have started to blur.

In this paper we describe the new Lagrangian hydrodynamics code MAGMA2, an SPH code that benefits from many improvements compared to more traditional SPH methods. It uses, for example, high-order kernels, calculates gradients via matrix-inversion techniques and uses slope-limited velocity reconstructions within an artificial viscosity approach. Many of these techniques have been scrutinised in a both Newtonian and special-relativistic context in Rosswog (2015a). The artificial viscosity approach that we are using is oriented at the recent work by Frontiere et al. (2017) which use fixed dissipation parameters, but reduce the effective viscosity by linearly reconstructing the velocities to inter-particle mid-points. In this paper we further expand on these ideas and throughout this paper we keep the dissipation parameters constant. We have also implemented a new way to steer time-dependent dissipation by monitoring local entropy violations and thus identifying “troubled particles” that need more dissipation. This new approach is discussed in a separate study (Rosswog 2020) and will not be used here. The main purpose of this paper is to document MAGMA2 as a new simulation tool and to demonstrate its performance in a series of benchmark tests.

The paper is structured as follows. In Sec. 2 we describe the methodology used in MAGMA2 and Sec. 3 is dedicated to benchmark tests. We begin with smooth advection, then various shock tests, subsequently explore Kelvin-Helmholtz and Rayleigh-Taylor instabilities and combined, vorticity-creating shocks. We conclude our test series with astrophysical tests such as stellar collisions and tidal disruption events that demonstrate the versatility, robustness and the excellent conservation properties in practical examples. Sec. 4 briefly summarises our study.

2 METHODOLOGY

Many of the design choices in MAGMA2 are informed by our recent work (Rosswog 2015a) where we have carefully explored various SPH ingredients such as the calculation of gradients, dissipation triggers or kernel functions. Methods that have been described in detail elsewhere are only briefly summarised, while we focus here on those elements that are new.

For a general introduction to the Smooth Particle Hydrodynamics (SPH) method, we refer to review articles (Monaghan 2005; Springel 2010b; Price 2012; Rosswog 2015b), a detailed step-by-step derivation of both Newtonian and relativistic SPH can be found in Rosswog (2009).

2.1 Ideal hydrodynamics

There are many different correctly symmetrised SPH discretizations of the ideal fluid equations. We have implemented three different SPH formulations into MAGMA2, which we briefly summarise below. For all of them we use high-order kernels and a novel dissipation scheme, but the formulations differ in the way gradients are calculated (two use matrix inversions, one kernel gradients), and in the symmetrisation of the equations.

2.1.1 Matrix inversion formulation 1 (MI1)

The standard SPH-approach of using direct gradients of (radial) kernel functions is a straight-forward way to ensure exact conservation¹. The resulting gradients, however, are of moderate accuracy only (Abel 2011; Garcia-Senz et al. 2012; Cabezon et al. 2012; Rosswog 2015a,b; Cabezon et al. 2017). Improvements of many orders of magnitude in gradient accuracy can be achieved, see Fig. 1 in Rosswog (2015a) at the (low) price of inverting a 3x3-matrix (in 3D).

The first matrix inversion formulation MI1 is the Newtonian limit of a special-relativistic formulation that was derived and extensively tested in Rosswog (2015a)². It reads explicitly:

$$\rho_a = \sum_b m_b W_{ab}(h_a), \quad (1)$$

$$\frac{d\vec{v}_a}{dt} = -\sum_b m_b \left\{ \frac{P_a}{\rho_a^2} \vec{G}_a + \frac{P_b}{\rho_b^2} \vec{G}_b \right\}, \quad (2)$$

$$\left(\frac{du_a}{dt} \right) = \frac{P_a}{\rho_a^2} \sum_b m_b \vec{v}_{ab} \cdot \vec{G}_a, \quad (3)$$

where ρ, \vec{v}, u and h denote mass density, velocity, specific internal energy and smoothing length. The particle mass is denoted by m , P is the gas pressure, $\vec{v}_{ab} = \vec{v}_a - \vec{v}_b$ and W is the chosen SPH kernel function. The gradient functions are given by

$$\left(\vec{G}_a \right)^k = \sum_{d=1}^3 C^{kd}(\vec{r}_a, h_a) (\vec{r}_b - \vec{r}_a)^d W_{ab}(h_a), \quad (4)$$

$$\left(\vec{G}_b \right)^k = \sum_{d=1}^3 C^{kd}(\vec{r}_b, h_b) (\vec{r}_b - \vec{r}_a)^d W_{ab}(h_b), \quad (5)$$

where $W_{ab}(h) = W(|\vec{r}_a - \vec{r}_b|, h)$. The “correction matrix” C accounts for the local particle distribution and is calculated as

$$\left(C^{ki}(\vec{r}, h) \right) = \left(\sum_b \frac{m_b}{\rho_b} (\vec{r}_b - \vec{r})^k (\vec{r}_b - \vec{r})^i W(|\vec{r} - \vec{r}_b|, h) \right)^{-1}. \quad (6)$$

The functions \vec{G}_k are anti-symmetric with respect to the exchange of the involved position vectors and therefore allow for exact conservation in a similar way as the anti-symmetric $\nabla_a W_{ab}$ in standard SPH. For more details we refer to Rosswog (2015a). The practical conservation will be scrutinised below in a violent, off-center collision between two stars, see Sec. 3.7.3, which shows that conservation with matrix inversion gradients is on par with standard SPH.

2.1.2 Matrix inversion formulation 2 (MI2)

The key property of the SPH-equations to achieve conservation, is to ensure the correct (anti-) symmetries in the particle indices, see for example Sec. 2.4 in Rosswog (2009) for detailed explanation. This can be achieved in an infinite number of different ways. One

¹ See e.g. Sec.2.4 of Rosswog (2009) for detailed discussion of conservation in SPH. “Exact conservation” means up to potential violations due to finite accuracy due to time integration or approximations of the gravitational forces, e.g. due to the use of a tree. These latter terms, however, are usually fully controllable, though at some computational expense.
² The corresponding formulation was called \mathcal{F}_3 in the original paper.

can, for example, start from the Lagrangian form of the Euler equations and use (Monaghan 1992)

$$\frac{\nabla P}{\rho} = \frac{P}{\rho^\sigma} \nabla \left(\frac{1}{\rho^{1-\sigma}} \right) + \frac{1}{\rho^{2-\sigma}} \nabla \left(\frac{P}{\rho^{\sigma-1}} \right), \quad (7)$$

where σ is real parameter. This leads to a momentum equation of the form

$$\frac{d\vec{v}_a}{dt} = - \sum_b m_b \left[\frac{P_a}{\rho_a^\sigma \rho_b^{2-\sigma}} + \frac{P_b}{\rho_a^{2-\sigma} \rho_b^\sigma} \right] \nabla_a W_{ab}, \quad (8)$$

and

$$\frac{du_a}{dt} = \frac{P_a}{\rho_a^\sigma} \sum_b m_b \frac{\vec{v}_{ab}}{\rho_b^{2-\sigma}} \nabla_a W_{ab}. \quad (9)$$

as an energy equation. We implement these equations, as in Sec. 2.1.1, by replacing the kernel gradients by the functions Eqs. (4) and (5). In the tests shown below we use $\sigma = 1$, so that final equations read

$$\frac{d\vec{v}_a}{dt} = - \sum_b m_b \left\{ \frac{P_a + P_b}{\rho_a \rho_b} \right\} \vec{G}_{ab}, \quad (10)$$

$$\left(\frac{du_a}{dt} \right) = \sum_b m_b \left\{ \frac{P_a}{\rho_a \rho_b} \right\} \vec{v}_{ab} \cdot \vec{G}_{ab}, \quad (11)$$

where $\vec{G}_{ab} = 0.5(\vec{G}_a + \vec{G}_b)$ and we use the density estimate of Eq. (1)³. If one replaces the matrix inversion gradient functions \vec{G} by the corresponding kernel gradients one recovers the SPH equations that have been successfully used in the Gasoline2 code (Wadsley et al. 2017).

While both of the matrix inversion formulations MI1 and MI2 yield very similar results on most benchmark tests, they show noticeable differences in some of them, for example in the Sedov explosion and in the "square test", see below. Where the results are practically indistinguishable, we will only show one set of results, only where visible differences occur will we show plots for different formulations.

2.1.3 Standard kernel gradient formulation (stdGrad)

For comparison purposes we have also implemented a more conventional kernel-gradient formulation

$$\frac{d\vec{v}_a}{dt} = - \sum_b m_b \left\{ \frac{P_a}{\rho_a^2} \nabla_a W_{ab}(h_a) + \frac{P_b}{\rho_b^2} \nabla_b W_{ab}(h_b) \right\}, \quad (12)$$

$$\frac{du_a}{dt} = \frac{P_a}{\rho_a^2} \sum_b m_b \vec{v}_{ab} \cdot \nabla_a W_{ab}(h_a), \quad (13)$$

where the density is calculated as in our default version, see Eq. (1). This equation set can be derived from a Lagrangian (Monaghan & Price 2001; Springel & Hernquist 2002), but note that we have for simplicity omitted the so-called "grad-h terms" that contain derivatives of the kernel with respect to the smoothing length. These terms further improve the numerical conservation, but our tests in Rosswog & Price (2007) have shown that the violations of exact conservation are very small, even under conditions that are considered as "worst case" (Hernquist 1993). This will be further confirmed in our collision test in Sec. 3.7.3 which demonstrates that conservation is excellent even without these correction terms.

³ We had also performed some experiments with $\sigma = 0$ and $\sigma = 2$, which give good, but slightly worse results in Sedov explosions than $\sigma = 1$.

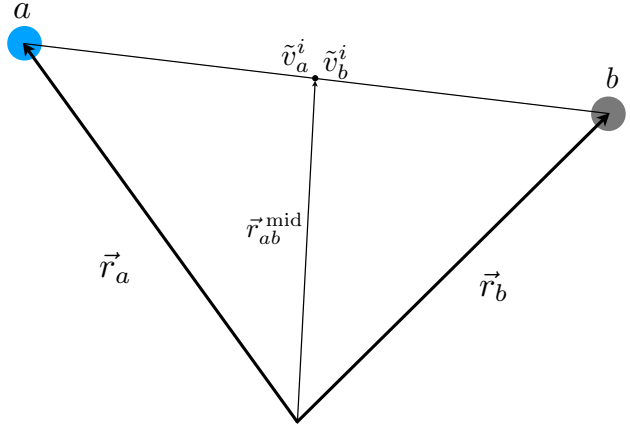


Figure 1. The artificial dissipation scheme uses the difference of the velocities reconstructed from particle a and particle b to their inter-particle midpoint at \vec{r}_{ab} .

2.2 Dissipation with reconstruction and slope-limiting

2.2.1 Artificial viscosity

A common approach to deal with shocks is to enhance the physical pressure P by additional viscous pressure terms Q (von Neumann & Richtmyer 1950), i.e. to replace the physical pressure, wherever it occurs, by $P + Q$. The pressures Q are typically the sum two terms, one is proportional to the velocity jump between computational elements (either cells or particles) while the other is proportional to the square of the jump. In SPH, the expression for the viscous pressure at particle position a is often written as (Monaghan & Gingold 1983)

$$Q_a = \rho_a \left(-\alpha c_{s,a} \mu_a + \beta \mu_a^2 \right), \quad (14)$$

where the velocity jump is

$$\mu_a = \min \left(0, \frac{\sum_\delta v_{ab}^\delta \eta_a^\delta}{\eta_a^2 + \epsilon^2} \right). \quad (15)$$

Here, α, β and ϵ are numerical parameters (typical values are 1, 2 and 0.1), c_s is the sound speed and

$$\eta_a^\delta = \frac{(\vec{r}_a - \vec{r}_b)^\delta}{h_a}, \quad \eta_a^2 = \sum_\delta \eta_a^\delta \eta_a^\delta \quad (16)$$

are separations between particles, de-dimensionalised via the smoothing length h_a . We follow the convention that particles are labelled usually by a and b and we use greek letters to denote summation indices (such as the δ above).

In SPH it is common practice to use $v_{ab}^\delta = v_a^\delta - v_b^\delta$ in Eq. (15), i.e. one applies the velocity difference between the two particles. One can think of artificial dissipation as a simple way of solving an inter-particle Riemann problem (Monaghan 1997). Translated to the language of finite volume methods, the common practice of using straight forwardly the differences between particle velocities corresponds to a zeroth-order, or constant, velocity reconstruction. Zeroth-order reconstruction is known to introduce excessive dissipation in finite volume methods, but higher order reconstructions yield successively less dissipative numerical schemes. This idea is translated here into an SPH context. Most modern SPH implementations use time-dependent dissipation

4 Rosswog

parameters to avoid excessive and unnecessary dissipation (Morris & Monaghan 1997; Rosswog et al. 2000; Cullen & Dehnen 2010; Rosswog 2015a; Wadsley et al. 2017; Price et al. 2018; Rosswog 2020). Recently, Frontiere et al. (2017), following ideas from a Eulerian finite volume context (Christensen 1990), have explored an alternative refinement where the same form of artificial pressure, Eq. (14), is used, but the velocity is (in their approach linearly) reconstructed to the particle midpoint. While still being a simple artificial viscosity scheme their approach showed excellent performance even with fixed dissipation parameters α and β .

Instead of using the difference of the two velocities, we quadratically reconstruct the velocities of particle a and b to their midpoint at $\vec{r}_{ab}^{\text{mid}} = 0.5(\vec{r}_a + \vec{r}_b)$, see Fig. 1. The velocities reconstructed from particle a to the midpoint read

$$\vec{v}_a^i = \vec{v}_a^i + \Phi_{ab} \left[(\partial_j v^i) \delta^j + \frac{1}{2} (\partial_i \partial_m v^j) \delta^l \delta^m \right]_a, \quad (17)$$

where Φ_{ab} is a slope limiter, see below, the index at the square bracket indicates that the derivatives at the position of particle a are used and the increments from point a to the midpoint are $(\delta^i)_a = \frac{1}{2}(\vec{r}_b - \vec{r}_a)^i$. The reconstructed velocities from the b -side, \vec{v}_b^i , are calculated correspondingly, but now with derivatives at position b and increments $\delta_b^i = -\delta_a^i$. In Eq. (15) we use the difference in the *reconstructed* velocities, i.e. $\vec{v}_{ab}^\delta = \vec{v}_a^\delta - \vec{v}_b^\delta$. We calculate the first derivatives as in Rosswog (2015a)

$$(\partial_j v^i)_a = C_a^{jk} \sum_b \frac{m_b}{\rho_b} [v_b^j - v_a^j] (\vec{r}_b - \vec{r}_a)^k W_{ab}(h_a), \quad (18)$$

where C is the correction matrix from Eq. (6). For the second derivatives we proceed in two steps. First, we calculate an auxiliary gradient that does not require the density (Price 2004; Rosswog & Price 2007) and therefore can be conveniently calculated alongside the density loop

$$(\partial_j v^i)_a^{\text{aux}} \equiv D_a^{jk} \sum_b m_b (v_b^j - v_a^j) \partial_k W_{ab}(h_a), \quad (19)$$

where the corresponding density-independent correction matrix is given by

$$D_a^{jk} = \left\{ \sum_b m_b (\vec{r}_b - \vec{r}_a)^j \partial_k W_{ab}(h_a) \right\}^{-1}. \quad (20)$$

The second derivatives are then calculated by applying Eq. (18) to the auxiliary first derivatives $(\partial_j v^i)_a^{\text{aux}}$. While this procedure to calculate second derivatives still comes at some cost, it does not require an additional loop over the neighbour particles compared to just linear reconstruction.

We use a modification of van Leer's slope limiter (van Leer 1974; Frontiere et al. 2017)

$$\Phi_{ab} = \max \left[0, \min \left[1, \frac{4A_{ab}}{(1 + A_{ab})^2} \right] \right] \begin{cases} 1, & \text{if } \eta_{ab} > \eta_{\text{crit}} \\ e^{-\left(\frac{\eta_{ab} - \eta_{\text{crit}}}{0.2}\right)^2}, & \text{otherwise} \end{cases} \quad (21)$$

with

$$A_{ab} = \frac{\sum \delta\gamma (\partial_\delta v_a^\gamma) x_{ab}^\delta x_{ab}^\gamma}{\sum \delta\gamma (\partial_\delta v_b^\gamma) x_{ab}^\delta x_{ab}^\gamma} \quad (22)$$

where the x_{ab}^δ are the components of $\vec{r}_a - \vec{r}_b$ and

$$\eta_{ab} = \min(\eta_a, \eta_b) = \min \left(\frac{r_{ab}}{h_a}, \frac{r_{ab}}{h_b} \right) \text{ and } \eta_{\text{crit}} = \left(\frac{32\pi}{3N_{\text{nei}}} \right)^{1/3}, \quad (23)$$

with $r_{ab} = |\vec{r}_a - \vec{r}_b|$ and N_{nei} being the number of neighbours for the chosen kernel, see Sec. 2.3. This prescription yields excellent, oscillation-free shock results as we demonstrate below.

2.2.2 Artificial conductivity

The analogy with Riemann solvers (Monaghan 1997; Chow & Monaghan 1997; Price 2008) also suggests to include thermal conductivity in the artificial dissipation terms. Such approaches have been found advantageous in certain shock problems (Noh 1987; Rosswog & Price 2007), but –as with all artificial dissipation terms– one has to ensure that no unwanted side effects are introduced. We add an artificial conductivity term to our energy equation

$$\left(\frac{du_a}{dt} \right)_C = -\alpha_u \sum_b m_b \frac{v_{\text{sig},u}^{ab}}{\rho_{ab}} (\tilde{u}_a - \tilde{u}_b) \frac{|\vec{G}_a + \vec{G}_b|}{2}, \quad (24)$$

where for the standard gradient version the average of the \vec{G} -terms is replaced by $[\nabla_a W_{ab}(h_a) + \nabla_b W_{ab}(h_b)]/2$. As for the velocities in the artificial viscosity, we use the differences in the quadratically reconstructed internal energies at the interparticle midpoint, \tilde{u}_a and \tilde{u}_b , which are calculated analogously to the velocities. For the conductivity signal velocity we use

$$v_{\text{sig},u}^{ab} = (1 - iG) v_{\text{sig},nG}^{ab} + iG v_{\text{sig},G}^{ab}, \quad (25)$$

where iG is a flag indicating whether gravity is used ($iG = 1$) or not ($iG = 0$) and

$$v_{\text{sig},nG}^{ab} = \sqrt{\frac{|P_a - P_b|}{\rho_{ab}}} \quad \text{and} \quad v_{\text{sig},G}^{ab} = |\vec{v}_a - \vec{v}_b|. \quad (26)$$

These expressions are very similar to those used in the PHANTOM code (Price et al. 2018), but, as with the artificial viscosity terms, we are using here differences in the reconstructed velocities and internal energies (as indicated by tildes) rather than "flat" differences and matrix-inversion based gradient functions.

Throughout this study, we always use constant dissipation parameters $\alpha = 1$ and $\beta = 2\alpha$. As we will demonstrate below, and consistently with a similar approach in a reproducing kernel context (Frontiere et al. 2017), the described velocity reconstruction produces excellent results and reduces drastically unwanted effects of artificial viscosity. Nevertheless, one may still try to additionally steer the dissipation parameter α so that –if it safe to do so– it decays towards zero. A novel way of steering α via violations of exact entropy conservation has recently been explored in a separate study (Rosswog 2020). It has also been implemented in MAGMA2, but all test shown here use fixed parameter values to demonstrate how powerful the artificial viscosity approach with reconstructed quantities is.

Concerning the conductivity, we very much stay on a conservative side with only small conductivity effects: we choose a low value of $\alpha_u = 0.05$ as default choice, we use the difference of reconstructed u -values in Eq. (24) and we use a switch of signal velocities, see Eq. (26), to protect a hydrostatic equilibrium configuration from being destroyed by conductivity. As shown below, none of the tests is substantially impacted by conductivity, not even the Kelvin-Helmholtz tests, see Fig. 22 in Sec. 3.5.1, which were a major motivation for introducing conductivity in the first place. While on the time scales usually shown in standard tests (and also here), conductivity effects are hardly noticeable in MAGMA2 simulations, we do see some positive effects in the long term evolution of Kelvin-Helmholtz instabilities, where, without conductivity, the flow looks

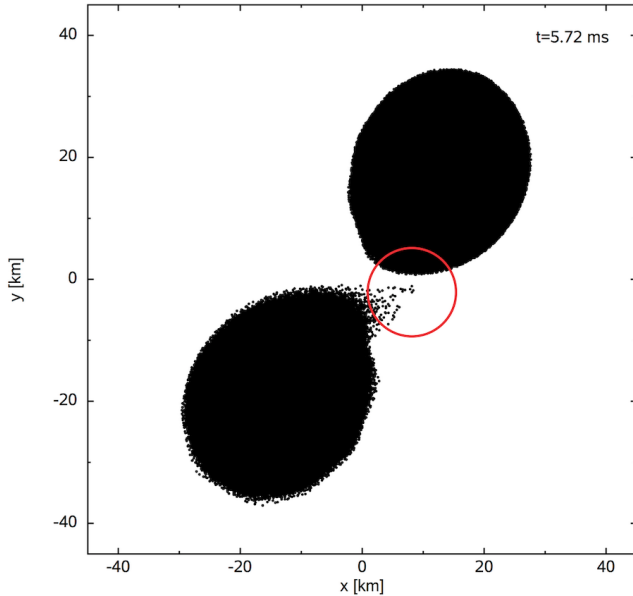


Figure 2. Astrophysical example (merger of a 1.3 with a 1.4 M_{\odot} neutron star) where an expanding flow encounters a sharp surface with a very large SPH particle density. The smoothing length of the leading particle is indicated by the red circle.

more granular. With our very conservative conductivity implementation we have not encountered any negative side effect, see for example, the test in Sec. 3.7.1. It is worth noting that Price et al. (2018) actually use a value of unity for α_u and report that they have not encountered artefacts for even this large value.

2.3 Kernel choice

SPH needs a kernel function to estimate densities and gradients, see Eqs.(1) - (13). Cubic spline kernels (Schoenberg 1946; Monaghan 2005) have traditionally been the standard choice in SPH. In recent years, however, a number of alternatives have been explored, see, for example, Cabezón et al. (2008); Read et al. (2010); Dehnen & Aly (2012); Rosswog (2015a). In particular the family of Wendland kernels (Wendland 1995) has received a fair amount of attention, because these kernels avoid the so-called “pairing instability” (Schüssler & Schmitt 1981) as pointed out by Dehnen & Aly (2012). While these kernels require a large neighbour number for an accurate density and gradient estimate, see Figs. 4 and 5 in Rosswog (2015a), they are exceptionally good at keeping an ordered particle distribution⁴ and in suppressing sub-resolution noise. We had experimented with other high-order kernels (Rosswog 2015a) and in static density and gradient estimation tests on fixed particle lattices they actually showed better accuracy than the Wendland kernels. In dynamic tests, however, the Wendland kernels delivered more ordered particle distributions and were overall the better choice. To illustrate this, compare the high-order $W_{h,9}$ and a C^6 Wendland kernel (WC6)⁵ in Figs. 4 and 11 in Rosswog (2015a). For these reasons we choose the WC6 kernel as a default

$$WC6(q) = \frac{\sigma}{h^3} (1-q)_+^8 \left(32q^3 + 25q^2 + 8q + 1 \right), \quad (27)$$

⁴ For an illustration see, e.g., Fig. 2 in Rosswog (2015b).

⁵ In the mathematical literature this kernel is referred to as $\Phi_{3,3}$.

where $\sigma = 1365/(512\pi)$ and $q = r/(2h)$. Note that for practical purposes/consistency with the other kernels in our module, we have written the kernel in a form so that it vanishes at $r/h = 2$. At every sub-step in the ODE integration we set the smoothing lengths so that there are exactly 300 contributing neighbours within the $2h_a$ -support of each particle a , see Sec. 2.5. This neighbour number is motivated by the tests shown in Figs. 4a and 5 in Rosswog (2015a). All tests in this paper use this combination of kernel and neighbour number.

2.4 Neighbour search and gravitational forces

We use a non-recursive tree that is based on “recursive coordinate bisection” (RCB) (Gafton & Rosswog 2011) to search for neighbour particles and to calculate gravitational forces. The main idea is to start from a cuboid that contains all the particles and then one recursively splits the longest side of each cuboid so that it contains (to high accuracy) the same number of particles in each resulting daughter cell. The procedure is repeated until, on the deepest level of the tree, each cell contains no more than N_{ll} particles. Such cells are referred to as lowest-level or ll-cells. We use $N_{ll} = 12$, but as shown in our original paper (Gafton & Rosswog 2011), the results are not very sensitive to this choice. Our tree yields very simple integer relations between different nodes in the tree, so that nodes can be addressed via simple integer arithmetics. The tree is not walked down for each particle, but instead only for each ll-cell. This means that the number of required tree-walks to find the neighbour particles is reduced by a factor of $\approx N_{ll}$. As a result of a neighbour tree walk, the tree returns a list of potential neighbour particles (“candidates”). Also for gravity, we only descend the tree for the centre of mass of each ll-cell, the forces at the particle positions within the ll-cell are obtained via a high-order Taylor-expansion. As shown in our original paper, this tree-build is for 4×10^6 particles approximately 30 faster than the Press tree (Benz et al. 1990). Neighbour search and gravity are at this particle number about a factor of 6 faster with our RCB with the discrepancy becoming increasingly larger for higher particle numbers N . Our RCB-tree scales close to $O(N)$ while the Press tree scales like most tree methods proportional to $O(N \log N)$.

Similar to the hydrodynamic equations, one can also derive the gravitational accelerations consistently from a Lagrangian (Price & Monaghan 2007) and the resulting equations contain corrective, “gravitational grad-h terms”. Consistent with our treatment of hydrodynamics, we also neglect the grad-h terms here, so that the gravitational acceleration reads

$$\left(\frac{d\vec{v}_a}{dt} \right)_{\text{grav}} = -G \sum_b m_b \left[\frac{\phi'_{ab}(h_a) + \phi'_{ab}(h_b)}{2} \right] \hat{e}_{ab}, \quad (28)$$

where $\hat{e}_{ab} = (\vec{r}_a - \vec{r}_b)/|\vec{r}_a - \vec{r}_b|$ and the gravitational potential that is used for monitoring the total energy

$$\Phi_a = G \sum_b m_b \phi_{ab}(h_a). \quad (29)$$

The gravitational smoothing kernel for the force, ϕ' , and for the gravitational potential, ϕ , can be calculated directly from the density kernel W via

$$\phi'(r, h) = \frac{4\pi}{r^2} \int_0^r W(r', h) r'^2 dr' \quad (30)$$

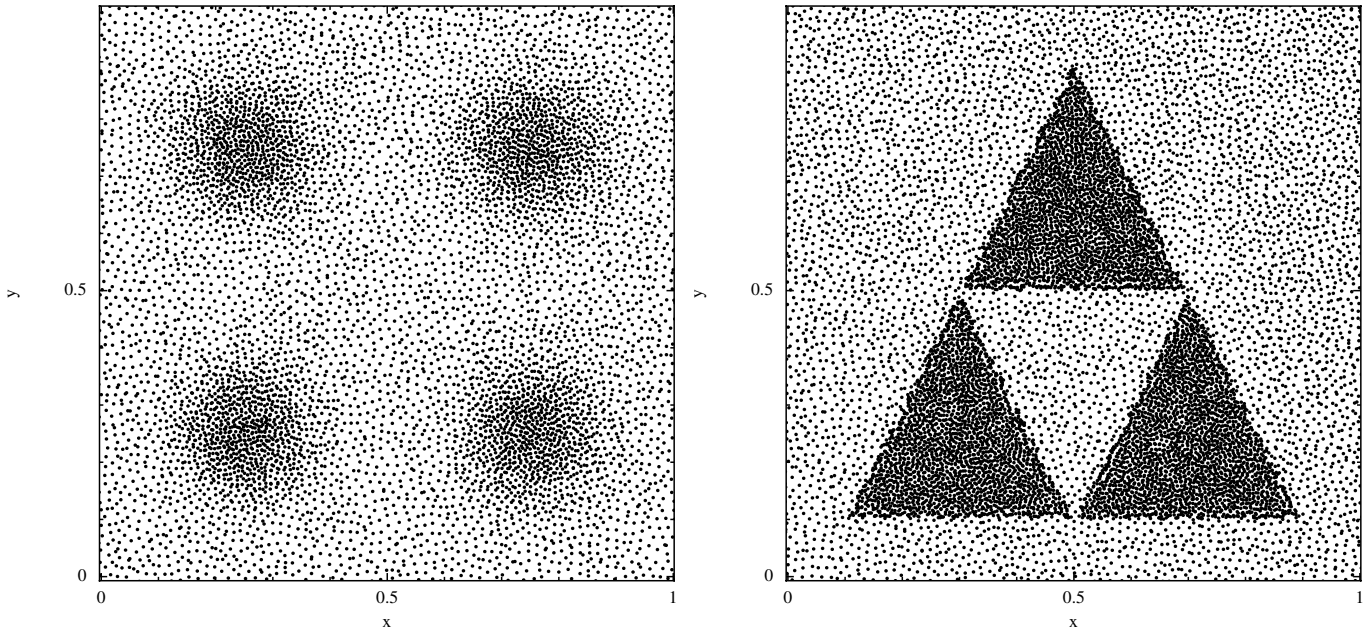


Figure 3. Two examples of "glass-like", equal-mass particle distributions that have been constructed with the "artificial pressure method" (APM). In this method, particles are assigned an artificial pressure value based on their current density error and, driven by hydrodynamics-type accelerations, gradients in these errors make the particles settle into a configuration that minimises this error. Left: superposition of four smooth Gaussian pulses, right: three triangles with enhanced density in their interior and sharp density transitions.

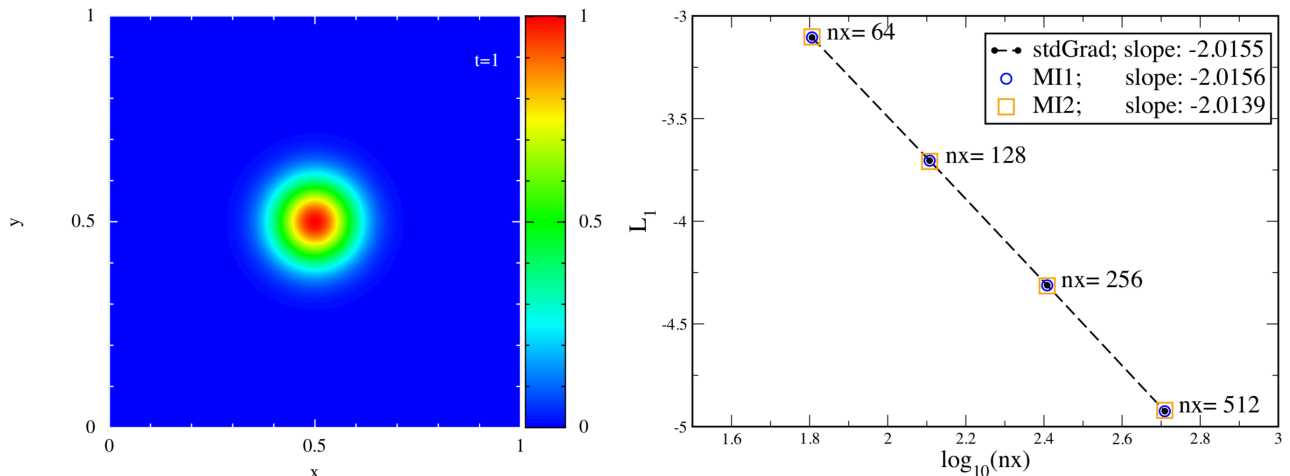


Figure 4. Advection of a smooth Gaussian pulse. Left: density distribution, right: L_1 -error as function of number of points in x-direction n_x for the kernel gradient (stdGrad) and the matrix-inversion versions (MI1, MI2). All three converge very close to the expected second order.

$$\varphi(r, h) = 4\pi \left[-\frac{1}{r} \int_0^r W(r', h) r'^2 dr' + \int_0^r W(r', h) r' dr' - \int_0^{Qh} W(r', h) r' dr' \right]. \quad (31)$$

For commonly used density kernels W these integrals can be solved analytically. However, to make it possible to change W with minimal modifications in the code, we calculate φ' and φ numerically and tabulate all kernels, so that for a different choice of W automatically the consistent kernels φ' and φ are available for force and potential calculation. As stressed in our original paper, large speed

gains have been obtained by mapping the tree variables into a "tree-vector" in exactly the order in which they are addressed during the tree-walk.

2.5 Adaption of smoothing lengths

The so-called "grad-h terms" (Springel & Hernquist 2002; Monaghan 2002) have been introduced in Newtonian, special- (Rosswog 2010a) and general-relativistic SPH (Rosswog 2010b) to ensure exact conservation. For pragmatic reasons, however, we set them here to unity since a consistent update of smoothing length

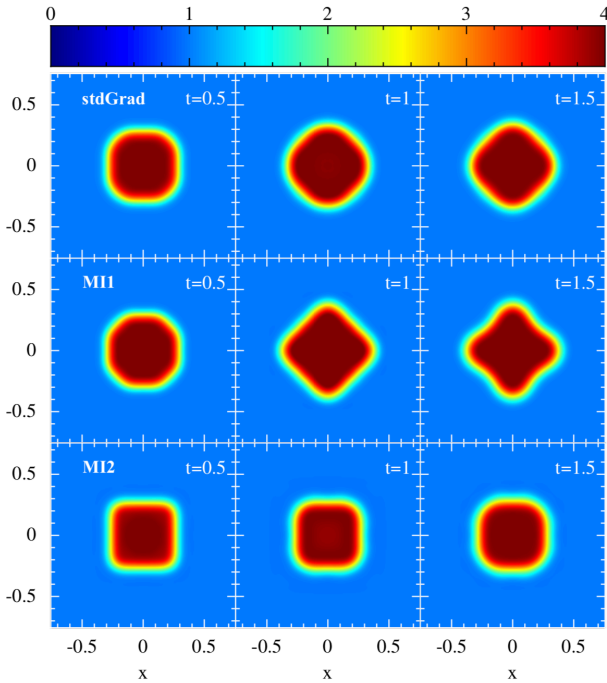


Figure 5. Results of a surface tension test (density) similar to Saitoh & Makino (2013). The upper row refers to the SPH-version with standard gradients, row two to the matrix inversion formulation 1, the lower row to the matrix inversion formulation 2 with a different symmetrisation of the SPH equations.

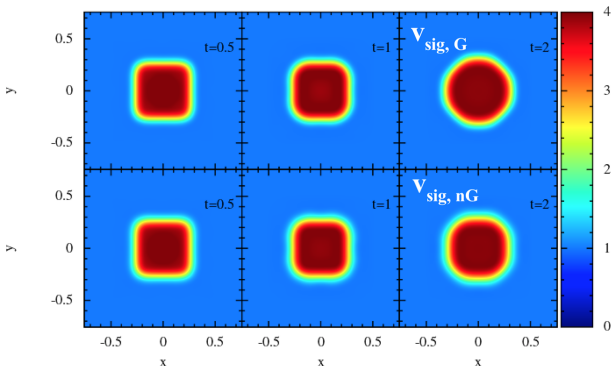


Figure 6. Same as previous figure, but the impact of varying the conductivity signal speed is shown (MI2). The top row uses $v_{\text{sig,G}}$, the bottom row $v_{\text{sig,nG}}$, see Sec.2.2.2.2.

and density requires an iteration between the two and this comes at a non-negligible computational expense. More importantly for us, our earlier experiments (Rosswog & Price 2007) showed that while the conservation properties improved somewhat, these were rather small corrections to an already excellent conservation. Even in a violent head-on collision of two stars, historically considered a “worst case scenario” for energy conservation in SPH (Hernquist 1993), the relative energy conservation was better than $\approx 10^{-3}$, even when ignoring the grad- h terms. These results are consistent with those presented below, see Sec. 3.7.3. Finally, and most relevant for our decision to *not* use an iteration between ρ and h , is that we kept running into numerical problems when an expanding flow suddenly encounters a sharp surface with a very large number density of SPH particles. Such an example, the merger of two neutron

stars with 1.3 and 1.4 M_{\odot} is shown in Fig 2: the density of the first particles that flow over the inner Lagrange point towards the heavier neutron star drops rapidly, thereby causing a strong increase in the smoothing lengths. Once close enough, the particles suddenly encounter the other neutron star with an enormous particle number density. It is a challenge to assign a good value for the smoothing length h of such front particles since a tiny change in h can easily change the neighbour number by an order of magnitude. This can lead to problems with the size of neighbour lists or—in case counter measures are taken—this can lead to very erratic changes of the smoothing length of this particle and therefore to a substantial amount of numerical noise.

To avoid such problems, we assign to each particle an exact neighbour number before its force is calculated. Consistent with our SPH equations, we consider as “neighbours” of particle a all those particles that are in the kernel support of $2h_a$, where h is the smoothing length. We first build our RCB-tree with smoothing lengths that are 10% larger than those from the previous time step. A neighbour tree walk then returns a substantially longer candidate list for each “lowest-level cell” than the desired neighbour number n_{des} of each particle. From this candidate list the particle with the $(n_{\text{des}} + 1)$ th largest distance, $d_a^{n_{\text{des}}+1}$, to the particle of interest a is selected via a partitioning algorithm (Press et al. 1992) and this distance sets the smoothing length: $h_a = 0.5d_a^{n_{\text{des}}+1}$ (keep in mind that all our kernels are scaled so that they have a support size of $r/h = 2$).

Although this algorithm may seem at first sight very computationally expensive, it is actually not: if we calculate all the derivatives needed for an SPH simulation for the case of a star made of 5×10^6 particles, the assignment of the smoothing length takes only $\approx 7\%$ of the total time to calculate the derivatives (usually dominated by self-gravity). Apart from being very robust in extreme situations, this procedure has the additional advantage that the smoothing lengths evolve very smoothly and without introducing unnecessary noise.

2.6 Time integration

We perform all shown tests with the total variation diminishing (TVD) second order Runge-Kutta (RK2) method (Gottlieb & Shu 1998)

$$y^* = y^n + \Delta t f(y^n) \quad (32)$$

$$y^{n+1} = \frac{1}{2} [y^n + y^* + \Delta t f(y^*)]. \quad (33)$$

If desired, the derivatives $f(y^*)$ can be “recycled” for the next prediction step, so that only one derivative is effectively calculated per time step. We have implemented this option as a simple switch, so that we can choose whether one or two derivatives are calculated per time step. We have explored the accuracy of this “force-recycling” in practical tests, but have not found noticeable differences in any of them. Nevertheless, we use the TVD RK2 integrator with two derivative calculations in the tests presented below.

The time step is chosen as minimum from a “force-” and “Courant-criterion” (Monaghan 1992)

$$\Delta t = C \min(\Delta t_f, \Delta t_C) \quad (34)$$

where

$$\Delta t_f = \min_a \left(\sqrt{\frac{h_a}{|\vec{f}_a|}} \right), \quad (35)$$

$$\Delta t_C = \min_a \left(\frac{h_a}{c_a + 0.6\alpha(c_a + 2\tilde{\mu}_a)} \right), \quad (36)$$

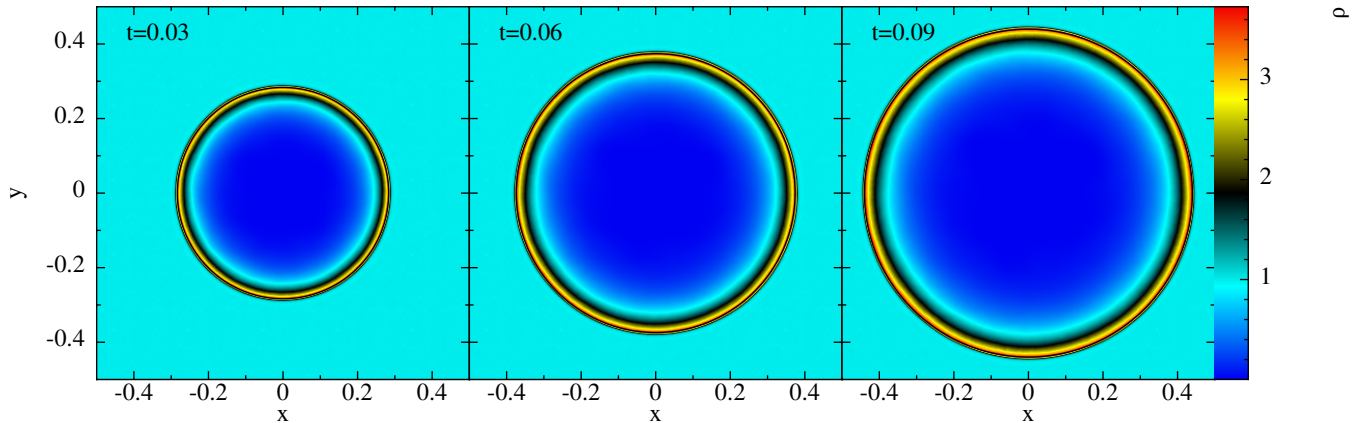


Figure 7. Time evolution of a 3D Sedov blast (256^3 particles). Colour coded is the density in xy -plane, the black circle at the leading edge of the blast is the analytical shock position. Note the absence of any visible deviations from spherical symmetry.

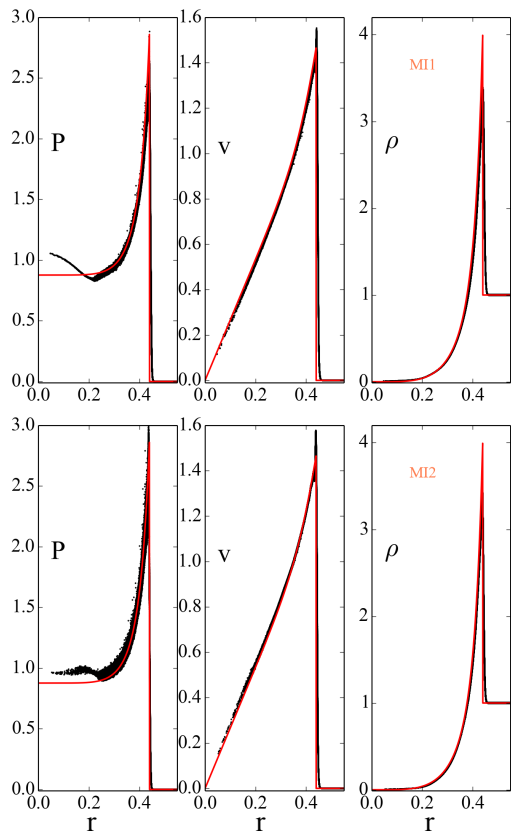


Figure 8. Sedov blast (200^3 particles) for different SPH-symmetrisations (matrix inversion formulation MI1 and MI2). The red lines denote the exact solution, the black dots are the numerical MAGMA2 results.

where $\tilde{\mu}_a = \max_b \left[h_a \tilde{v}_{ab}^\delta r_{ab}^\delta / (r_{ab}^2 + 0.01) \right]$ and for the prefactor we choose $C = 0.2$. While being very simple and efficient, this time integration algorithm provides excellent numerical conservation of energy and angular momentum, as we will show below.

We restrict ourselves for now to a global time step for all particles. Obviously, for problems with a large range of different possible time steps among the particles, one can substantially reduce the

computing time by allowing for individual time steps. This comes, however, at a price. It makes the code more involved due to the time step book-keeping, it deteriorates the conservation properties and if the time step bins between neighbouring particles are not restricted properly, particles can “be surprised”, say, by an approaching blast wave and this can lead to wrong results (Saitoh & Makino 2009). Individual time steps make it also more cumbersome to remove particles, say, in an accretion process. For all these reasons we stick for now with a global time step, but if future problems will require it, we will implement an integration scheme with individual time steps.

2.7 Implementation

MAGMA2 has been written from scratch in clean and modular Fortran 95/2003. We have paid particular attention to separate technical infrastructure (such as the tree for neighbour search) from the physical modules. MAGMA2 uses exclusively double precision and much attention has been paid to keep the “hot loops” fast. This is of particular importance for MAGMA2 since due to the large neighbour number the density and hydrodynamic derivative loops become computationally very expensive. The strategy is to analyze in which order different variables are addressed in the expensive loops and to map them exactly in this order in “cache arrays”, very similar to how this is done within our RCB-tree, see for example Sec. 2.2.1 in Gafton & Rosswog (2011). To keep the code clean and (relatively) simple, we have so far only included a global time step for all particles. At the current stage, MAGMA2 is parallelised with OpenMP and is able to perform tests (global time step, 2nd order Runge-Kutta and 300 neighbour particles) with $\sim 10^8$ SPH particles when no self-gravity is involved and a few 10^7 otherwise (e.g. on Intel Skylake Gold compute nodes). Further performance improvements are a subject for the future.

3 TESTS

We begin with an advection test to measure the order of convergence in smooth flows. We then show a number of shocks, a Kelvin-Helmholtz and a Rayleigh-Taylor instability test. We further show combined tests where shocks go along with vorticity

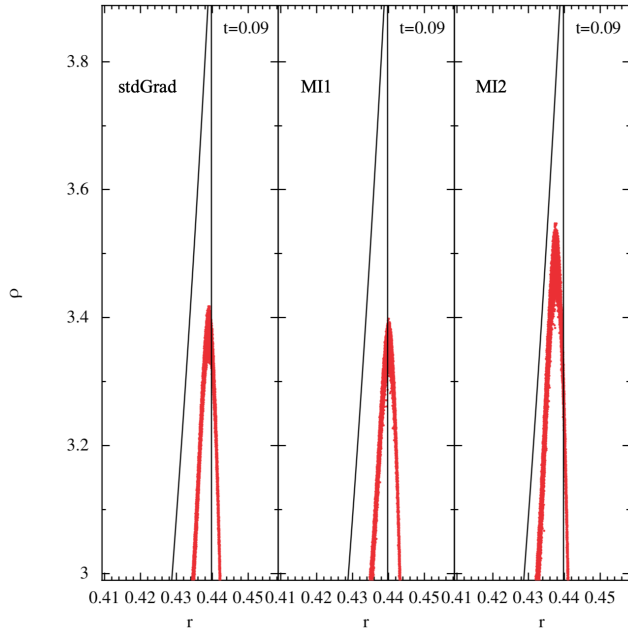


Figure 9. Comparison of the density peak height (200^3 particles) for the kernel- (stdGrad) and the two matrix-inversion formulations (MI1, MI2).

creation (“Schulz-Rinne tests”) and we conclude with astrophysical tests, a stellar collision and a tidal disruption, that demonstrate MAGMA2’s robustness for practical applications.

All of the tests shown below are performed with the full 3D code. “2D” tests are performed by simulating a slice that is thick enough for the central plane not to be affected by edge effects.

3.1 Initial conditions: the Artificial Pressure Method (APM)

As pointed out earlier (Rosswog 2015a) good initial conditions are crucial for obtaining accurate results in SPH simulations, but unfortunately it is sometimes non-trivial to construct initial conditions with all the desired properties. The particles should be distributed with high regularity so that they guarantee a high interpolation accuracy (see, e.g., Sec. 3 of Rosswog (2015a) for an accurate interpolation quality indicators). This is, however, not enough, since the particle distribution should also not contain any preferred directions, but simple lattices usually do. This may lead to artefacts such as the piling up of particles in a shock (“particle ringing”) along the grid direction, see Fig. 17 in Rosswog (2015a) for an illustration. Setting up SPH-initial conditions for a prescribed non-constant density distribution can become challenging. The simplest approach is to start with some regular lattice, say a cubic lattice (CL) or (better) a “close-packed” (CP) lattice, and assign particle masses so that the desired density is reproduced. For small density differences this delivers acceptable results, but for large density contrasts this results in particles with very different masses and this is known to introduce unwanted noise into simulations, see e.g. Lombardi et al. (1999). Setting up configurations with equal mass particles would be desirable, but it is substantially more challenging since the particles need to be placed in a way so that their local number density reflects the desired mass density. For simple cases, stretching a uniform lattice to the desired density distribution can be used, e.g. Rosswog et al. (2009); Price et al. (2018). For more general cases methods based on Centroidal Voronoi Tessellations have been

suggested Diehl et al. (2012).

Here we suggest a novel approach that is very close to the spirit of SPH. The idea is to start from an SPH-like momentum equation that uses artificial pressures, \tilde{P}_a , which are based on the current density error. If the density estimated by all particles is in perfect agreement with the desired density profile, all particles have the same pressure and will therefore not feel a net force. If in contrast, density errors exist, then the gradients in the artificial pressures drive the equal mass particles into positions that minimise density errors. Rather than actually integrating this artificial equation, we use a Courant-type time step to translate the ordinary differential equation into a position update formula for each particle, $\vec{r}_a \rightarrow \vec{r}_a + \Delta\vec{r}_a$. Once a particle has reached an optimal position, the pressure gradient vanishes and it stays at the reached position.

Assume that we start from an initial distribution of equal mass particles whose mass m has been calculated from the desired density profile $\rho^P(\vec{r})$ and the number of particles. As a next step we measure the densities at the particle positions, ρ_a , via Eq. (1) and then assign to each particle an artificial pressure based on its relative density error:

$$\tilde{P}_a = P_0 \left(\max \left[1 + \frac{\rho_a - \rho^P(\vec{r}_a)}{\rho^P(\vec{r}_a)}, 0.1 \right] \right) \equiv P_0 \Pi_a, \quad (37)$$

where P_0 is a so far arbitrary base pressure and the max-function avoids negative pressures as they might otherwise occur for bad initial guesses. This means that particles with too low (too high) density estimates have smaller (larger) pressures and therefore more particles will move into (out of) this region. With these artificial pressures we construct an SPH-type momentum equation (similar to Eq. (8))

$$\vec{f}_a^{APM} = -mP_0 \sum_b \frac{\Pi_a + \Pi_b}{\rho_a \rho_b} \nabla_a W_{ab}(h_a), \quad (38)$$

and we now choose a Courant-type time step

$$\Delta t_a^{APM} \propto \frac{h_a}{c_{s,a}} \propto h_a \sqrt{\frac{\rho_a}{P_0}}, \quad (39)$$

where we have used the polytropic relation for the sound speed $c_s = \sqrt{\Gamma P / \rho}$. We obtain a dimensionally correct update formula by multiplying our acceleration formula Eq. (38) by $(\Delta t_a^{APM})^2$ so that the final position correction becomes

$$\Delta \vec{r}_a = -\xi h_a^2 m \sum_b \frac{\Pi_a + \Pi_b}{\rho_b} \nabla_a W_{ab}(h_a). \quad (40)$$

Note that the base pressure P_0 has dropped out. The prefactor ξ is not critical for the iteration process, but has some impact on how quickly the desired density profile is reached. After some experimenting we settled on a value of $\xi = 0.5$.

During the iteration process we monitor the maximum and average density error and

$$\delta P U_a \equiv 1 - \sum_b \frac{m_b}{\rho_b} W_{ab}(h_a), \quad (41)$$

to see by how much the particle distribution deviates from a perfect partition of unity at each particle position, see e.g. Sec. 2.1 in Rosswog (2015b) for a discussion of interpolation quality. As an example, in our setup of the Kelvin-Helmholtz problem, see below, we find after 500 iterations typically average density errors of a few times 10^{-3} with maximum deviations in transition regions of very few percent. The average $\delta P U_a$ values are at this point below 10^{-5} , so that we have an excellent interpolation quality. To further improve the agreement between the set up and the

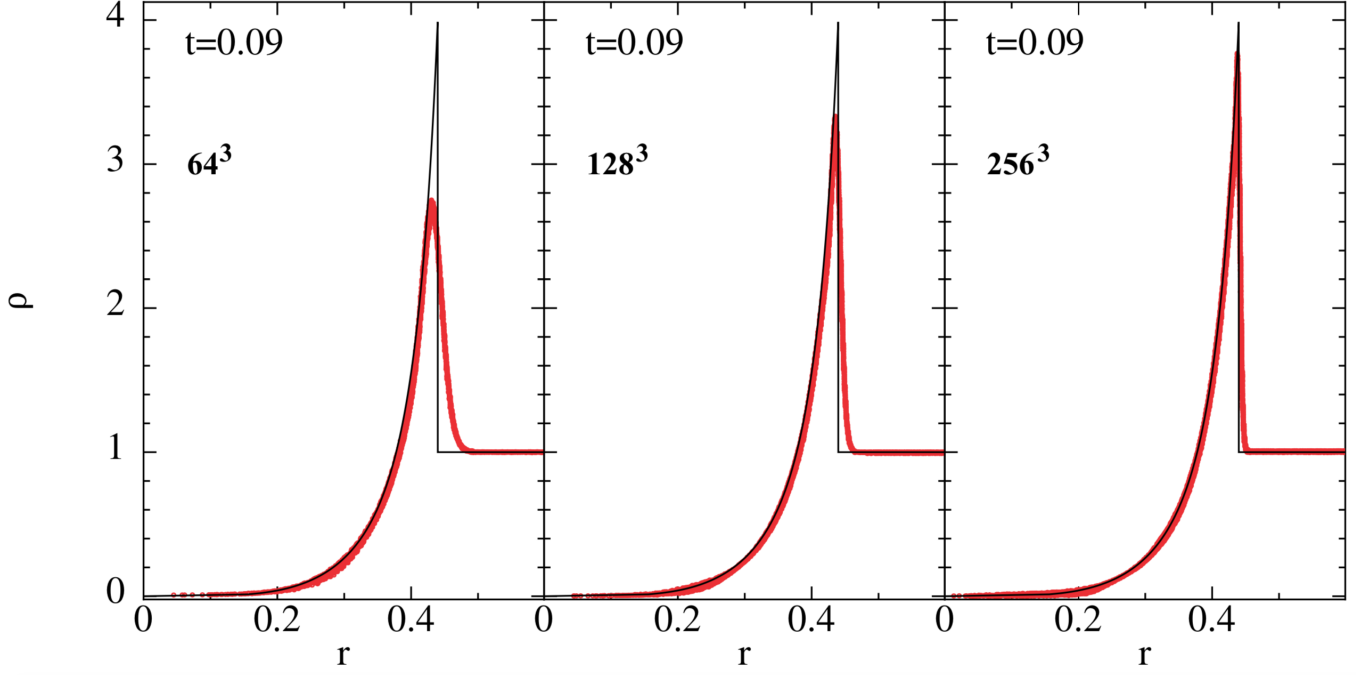


Figure 10. 3D Sedov blast of increasing resolution (64^3 , 128^3 , 256^3 particles; MI2 formulation), every single particle is plotted.

desired density profile after the iteration process has stopped, we measure the local SPH particle number density

$$n_a = \sum_b W_{ab}(h_a) \quad (42)$$

and assign final particle masses $m_a = \rho^P(\vec{r}_a)/n_a$, so that the setup contains particles that are to within percent level of the same mass. To illustrate the versatility of this method, we set up a non-trivial density profile with equal mass SPH particles. As density profile we choose

$$\rho^P(x, y) = \Delta\rho \sum_{j=1}^4 \exp\left\{-\frac{(x-x_j)^2 + (y-y_j)^2}{\sigma^2}\right\} + \rho_0, \quad (43)$$

where $\rho_0 = 1$, $\Delta\rho = 5$, $\sigma = 0.1$. We start by placing 20 layers (in z -direction) of 100×100 particles in $[-0.2, 1.2] \times [-0.2, 1.2]$ and we place six layers of "frozen" particles (which are not updated in the iteration process) as boundary conditions in the surrounding volume. The centres of the density pulses, (x_j, y_j) , are offset from the corners by 0.25. The particles are initially distributed on a cubic lattice and then randomised to erase the undesired lattice structure. The particle distribution ($|z| < 0.02$) after 1000 APM-iterations is shown in Fig. 3, left panel. The particles have settled into a "glass-like" structure with their number density reflecting the mass distribution.

As a second example, we set up sharp density profile that the particles try to approximate (within the limits of their finite resolution and uniform mass) as well as possible. For the density profile we choose

$$\rho^T(x, y) = \begin{cases} \rho_0 + \Delta\rho & \text{inside the outer, but not in inner triangle} \\ \rho_0 & \text{else,} \end{cases} \quad (44)$$

where the outer triangle refers to the interior of the points $(0.1, 0.1), (0.1, 0.9), (0.5, 0.9)$ and the inner triangle is given by

the midpoints of the outer triangle's sides and we use $\rho_0 = 1$ and $\Delta\rho = 5$, as before. The particles are initially placed as in the previous example and their distribution after 1000 APM-iterations ($|z| < 0.02$) is shown in Fig. 3, right panel. Note that in all regions the particles have arranged into uniform glasses with sharp transitions between the different regions.

While the method is very flexible and powerful, it costs some computational effort: each iteration requires a density loop with the corresponding neighbour search. We therefore stick to the pragmatic approach that we use simpler particle setups where this delivers good results.

3.2 Smooth advection

In this test we place a Gaussian density pulse of initial shape

$$\rho^{\text{in}}(x, y) = (\rho_2 - \rho_1) \exp\left[-\frac{(x-0.5)^2 + (y-0.5)^2}{\sigma^2}\right] + \rho_1, \quad (45)$$

where $\rho_1 = 10^{-3}$, $\rho_2 = 1$ and $\sigma = 0.1$ in a (quasi)-2D box with $[0, 1] \times [0, 1]$, see Fig. 4, left panel. The gas with polytropic index $\Gamma = 5/3$ is represented by 20 CL-layers of $n_x \times n_x$ particles. The density profile is advected with uniform pressure $P_0 = 10^{-6}$ and velocity $v_x = 1$ through the box with periodic boundaries. After crossing the box once the L_1 -error, $L_1 = \sum_b^N |\rho^{\text{in}}(\vec{r}_b) - \rho_b|/N$, is measured. The L_1 -results for different resolutions n_x are plotted in the right panel of Fig. 4 for all of our three variants. The measured slopes are always very close to the 2nd order that is theoretically expected for our code.

3.3 Surface tension test

SPH has the peculiarity that density and internal energy can be of different smoothness: the density is calculated via Eq. (1), so

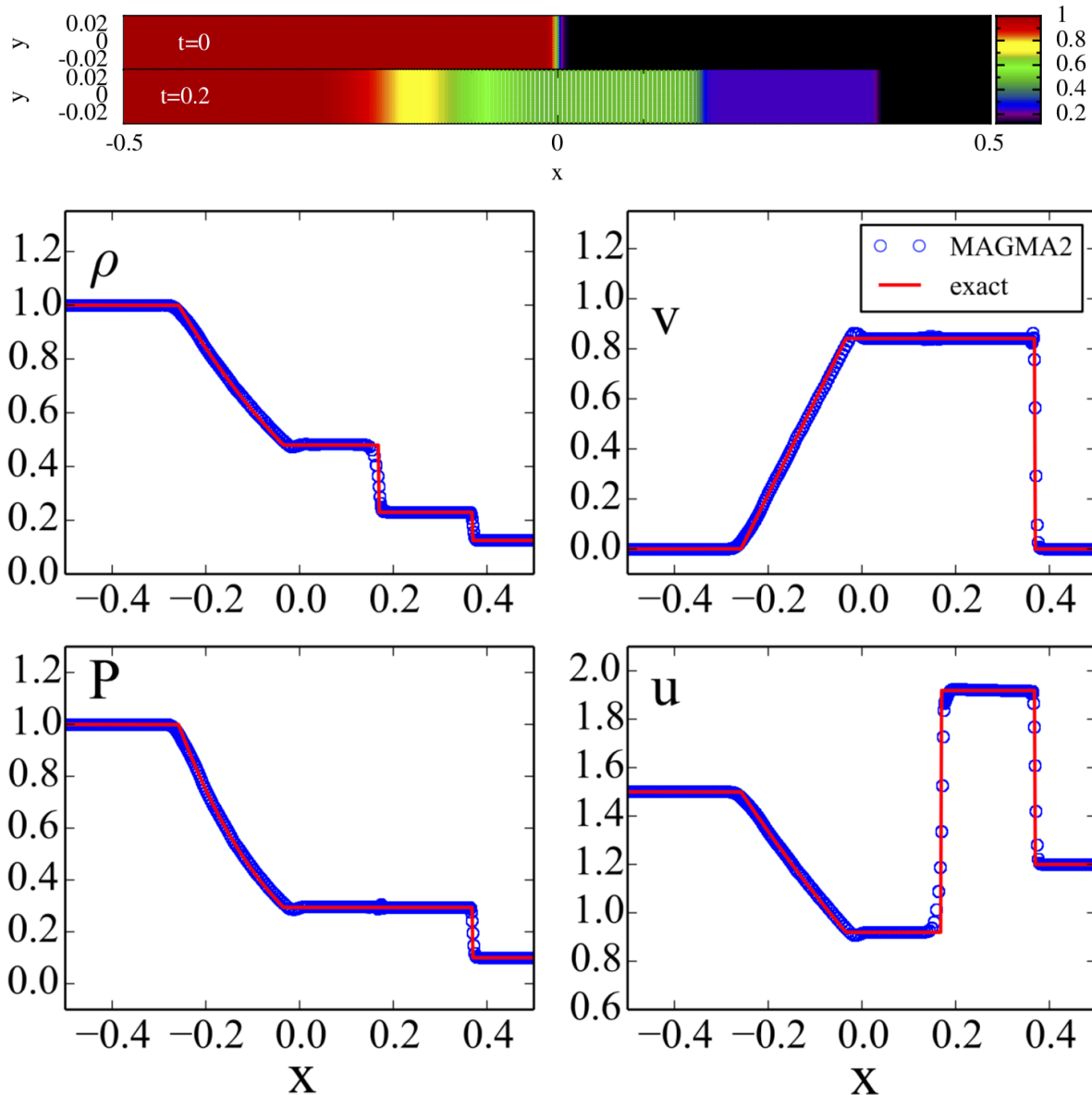


Figure 11. Sod shock test performed in 3D with $400 \times 24 \times 24$ particles. The upper two panels shows the particle distribution (density is colour-coded) at $t=0$ and $t=0.2$. The four panels below show (upper left to lower right) density, velocity, pressure and internal energy of all particles at $t=0.2$ together with the exact solution (red). All particles are plotted.

that even when there is a sharp transition in the particle masses the density transition is smooth. The internal energy equation, in contrast, is a straight-forward translation of the first law of thermodynamics and u is not necessarily smooth. If contact discontinuities, i.e. interfaces where both density and internal energy exhibit a discontinuity, but the pressure, $P = (\Gamma - 1)\rho u$, is continuous, are not set up carefully, spurious pressure gradients can emerge which lead to unwanted "surface tension effects" (Springel 2010b; Heß & Springel 2010). In the worst case, this can suppress weak instabilities (Agertz et al. 2007).

We set up a surface tension test similar to Saitoh & Makino (2013) and compare the performance of our three different SPH formulations. We place 40^3 particles on a cubic lattice with spacing Δ within $[-0.5, 0.5]^3$ and assign them masses $m_a = \tilde{\rho}(\vec{r}_a)\Delta^3$ with a

sharp transition according to

$$\tilde{\rho}(x, y, z) = \begin{cases} 4 & \text{for } -0.25 < x, y, z < 0.25 \\ 1 & \text{otherwise} \end{cases}$$

to test for the presence of spurious forces. Note, however, that this is *not* how we would usually set up reliable simulation. We then calculate the density according to Eq. (1) and assign the internal energies according to $u_a = P_0/(\Gamma - 1)\rho_a$. Following Saitoh & Makino (2013) we use constant pressure $P_0 = 2.5$ everywhere.

The results for the different SPH formulations are shown in Fig. 5. Both the standard gradient version (top row) and the MI1 formulation show (with this somewhat pathological test setup) clear signs of surface tension. The MI2 formulation performs by far best, but is still not entirely free of surface tension effects (at least for this setup with a sharp mass transition). Here further progress could be obtained by using volume elements that are different from $V_b = m_b/\rho_b$

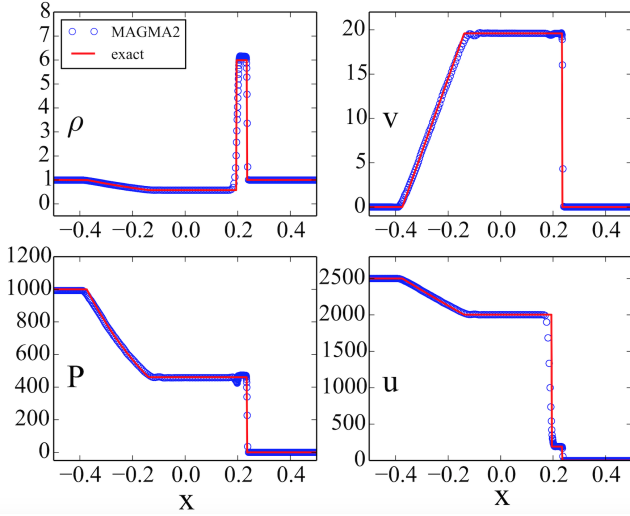


Figure 12. 3D strong blast wave test at $t = 0.01$ ($800 \times 24 \times 24$ particles).

(Saitoh & Makino 2013; Hopkins 2013; Rosswog 2015a; Cabezon et al. 2017). We also show the impact of varying the conductivity signal speed, see Fig. 6. Clearly, $v_{\text{sig,nG}}$ shows the better result, which argues for using the switch in Eq. (26). We note, however, that despite small possible surface tension effects both MI1 and MI2 formulations perform very well in the instability tests, see below.

3.4 Shocks

3.4.1 3D Sedov-Taylor explosion

The Sedov-Taylor explosion test, a strong, initially point-like blast into a low density environment, has an analytic self-similarity solution (Sedov 1959; Taylor 1950). For an explosion energy E and a density of the ambient medium ρ , the blast wave propagates after a time t to the radius $r(t) = \beta(Et^2/\rho)^{1/5}$, where β depends on the adiabatic exponent of the gas (≈ 1.15 in 3D for the $\Gamma = 5/3$ that we are using). Directly at the shock front, the density jumps by the strong-explosion limit factor of $\rho_2/\rho_1 = (\Gamma + 1)/(\Gamma - 1) = 4$, where the numerical value refers to our chosen Γ . Behind the shock the density drops quickly and finally vanishes at the centre of the explosion.

To set up the test numerically, we distribute a given number of SPH particles according to a *Centroidal Voronoi Tessellations* (CVT) (Du et al. 1999) in the computational volume $[-0.5, 0.5] \times [-0.5, 0.5] \times [-0.5, 0.5]$. While this produces already nearly perfect initial conditions, they can be further improved by additional sweeps according to Eq. (40). Even if the differences in the particle distributions are hard to see by eye, they still improve the outcome of the Sedov test. We use here 500 of such sweeps. Once the particle distribution is settled, we assign masses so that their density is $\rho = 1$. This is done in an iterative way where we first assign a guess value for the masses, then measure the resulting density via Eq. (1) and subsequently correct the particle masses. The iteration is stopped once the density agrees everywhere to better than 0.5% with the desired value. The energy $E = 1$ is spread across a very small initial radius R and it is entirely distributed as internal energy, the specific internal energy u of the particles outside of R is entirely negligible (10^{-10} of the central u). For the initial radius R we choose twice the interaction radius of the innermost SPH particle. Boundaries

play no role in this test as long as the blast does not interact with them. We therefore place “frozen” particles around the computational volume as boundary particles.

Fig. 7 shows the time evolution of the density for 256^3 particles for our MI2-formulation (the other formulations look virtually identical). The overall agreement with the exact solution (shock position is indicated by a black circle at shock front) is excellent and there are no noticeable deviations from spherical symmetry. We show in Fig. 8 comparisons of the solutions (pressure, velocity and density) obtained with the MI1 and MI2 formulations, the particle solutions are shown as black dots (downsampled by a factor of 10), the red lines indicates the exact solutions. Note in particular the absence of density and velocity oscillations in the wake of the shock. Such oscillations plague practically all (even modern) SPH-simulations of this test, see for example Rosswog & Price (2007); Hu et al. (2014); Cabezon et al. (2017); Wadsley et al. (2017); Frontiere et al. (2017), but they are virtually absent in our tests⁶. We attribute this to our carefully constructed initial conditions together with the use of a Wendland kernel with 300 neighbour particles.

Despite this overall very good agreement, a closer inspection shows some interesting differences that are due to different SPH symmetrisations (gradient accuracy plays a minor role in this test) see Fig. 8. The MI2-formulation seems to be substantially more sensitive to density variations which can be seen in a larger post-shock pressure variance, probably picking up on small density variations that are residuals of our iterative approach to set up the initial conditions. More importantly, MI2 reaches a noticeably larger density peak (apart from the symmetrisation everything else is exactly the same), see Fig. 9. Note also that the SPH-peak for the more commonly used symmetrisations (stdGrad and MI1) occurs at the shock-front while the MI2-case peaks between both lines indicating the exact solution. The MI2-symmetrisation result also captures the flat central pressure profile in a better way.

Obviously, the peak height could easily be raised by using a lower order kernel with fewer neighbours, if one was willing to accept more post-shock noise (which we are not). For completeness we also show Sedov tests (with MI2) with increasing resolution of 64^3 , 128^3 and 256^3 SPH particles within $[-0.5, 0.5]^3$, see Fig. 10.

3.4.2 3D Sod shock

The “Sod shock tube” (Sod 1978) is a classic code test to ensure the correctness of a hydrodynamics code implementation. As initial conditions we use

$$(\rho, \vec{v}, P) = \begin{cases} (1.000, 0, 0, 0, 1.0) & \text{for } x < 0. \\ (0.125, 0, 0, 0, 0.1) & \text{else.} \end{cases} \quad (46)$$

and $\Gamma = 5/3$. In most SPH papers this test is only shown in 1D. Here we perform a quasi-1D test with the 3D code, employing $400 \times 24 \times 24$ particles placed in $[-0.5, 0.5] \times [-0.03, 0.03] \times [-0.03, 0.03]$. Here even the simplest approach with particles placed on a uniform cubic lattice gives good results, see Fig. 11. The numerical results (all particles are shown) agree well with the exact solution, there is only a small velocity overshoot at the shock front and small over-/undershoots at one of the edges of the rarefaction region ($x \approx -0.05$). The plot shows the results of the MI1-formulation, there are no noteworthy differences between the different formulations for this test.

⁶ The PHANTOM code paper (Price et al. 2018) does not show velocities, but some oscillations are visible in the densities.

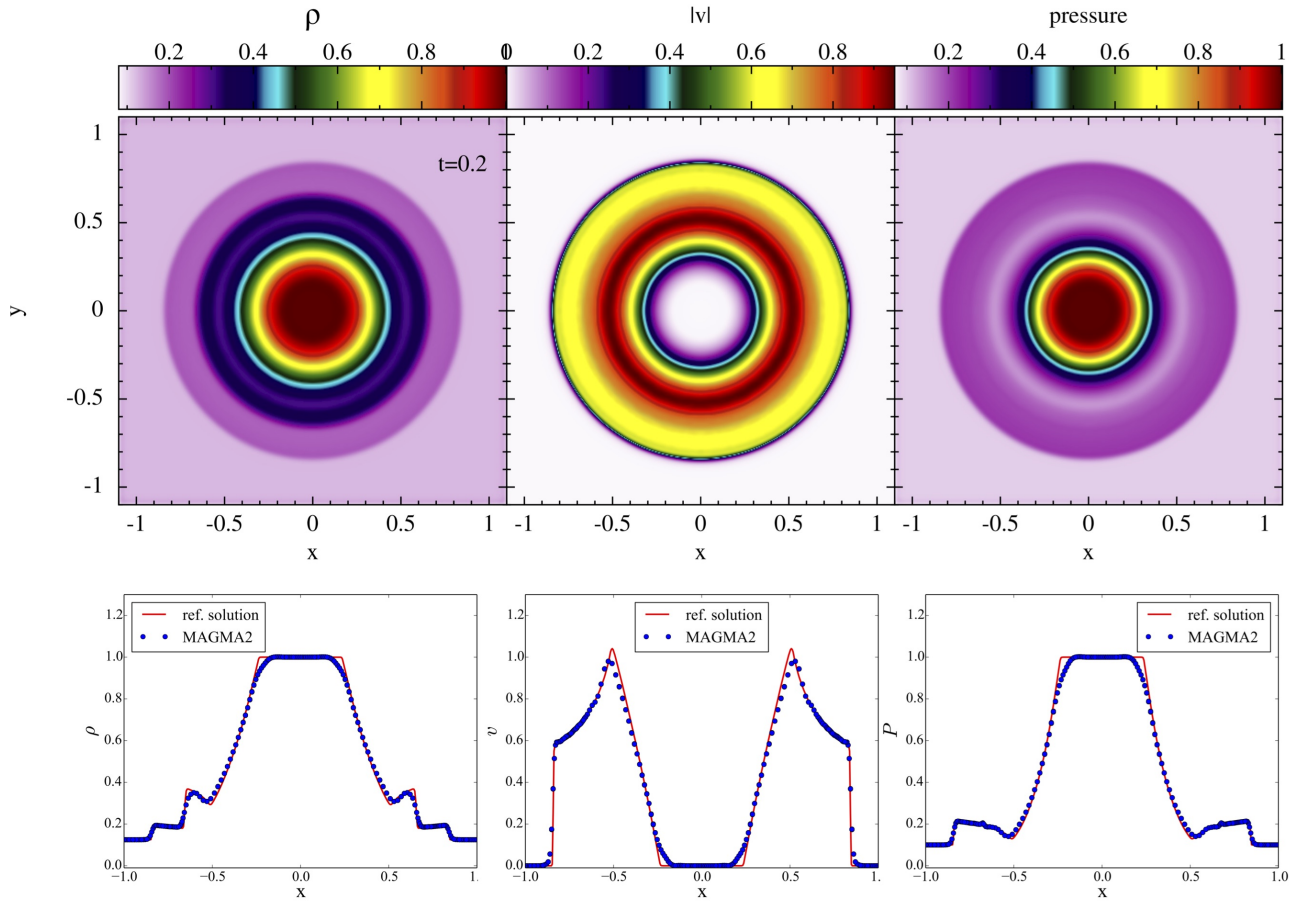


Figure 13. Circular blast wave problem 1 in 3D at $t = 0.2$ (200^3 particles). Upper row: MAGMA2 result for density, $|v|$ and pressure. Lower row: corresponding quantities from MAGMA2 results compared with a reference solution (red line) obtained by the Eulerian weighted average flux method (400^3 grid cells) (Toro 1999).

3.4.3 3D strong blast wave

A substantially more challenging version of the Sod test, the so-called strong blast wave test, is set up with initial conditions

$$(\rho, \vec{v}, P) = \begin{cases} (1.0, 0, 0, 0, 1000.0) & \text{for } x < 0 \\ (1.0, 0, 0, 0, 0.1) & \text{else} \end{cases} \quad (47)$$

and with $\Gamma = 1.4$. Again we set up this test as quasi-1D with our 3D code in an analogous way to the Sod test with $800 \times 24 \times 24$ particles between $[-0.5, 0.5]$ in x -direction. The result (obtained with MI1; no noteworthy differences for MI2 and stdGrad) at time $t = 0.01$ is shown in Fig. 12. Overall, the numerical result is in very good agreement with the exact solution, but there are small overshoot in density and dips in pressure and velocity at the contact discontinuity.

3.4.4 Spherical blast wave 1

As another benchmark we use a three-dimensional shock-tube problem. We follow Toro (1999) in the parameter choice (apart from a shift of the origin): the computational domain is $[-1, 1]^3$ and the initial conditions are chosen as:

$$(\rho, \vec{v}, P) = \begin{cases} (1.000, 0, 0, 0, 1.0) & \text{for } r < 0.5 \\ (0.125, 0, 0, 0, 0.1) & \text{else.} \end{cases} \quad (48)$$

The solution exhibits a spherical shock wave, a spherical contact surface traveling in the same direction and a spherical rarefaction wave traveling towards the origin. We show the MAGMA2 solution (200^3 particles, cubic lattice; shown is MI1, other formulations nearly identical) at time $t = 0.2$ in Fig. 13. We show in the upper row the density, $|v|$ and pressure at $t = 0.2$ in the XY -plane. In the lower row, we compare the SPH-result ($|y| < 0.018, |z| < 0.018$) with a reference solution obtained by the Eulerian weighted average flux method with 400^3 grid cells (Toro 1999). The SPH solution is essentially oscillation-free and in very close agreement with the reference solution. Only the sharp edges (e.g. in $|v|$ near $|x| \approx 0.3$) are somewhat smoothed out and there is a small oscillation in the pressure at the contact discontinuity.

3.4.5 Spherical blast wave 2

As a second spherical blast wave problem (Toro 1999) we start from

$$(\rho, \vec{v}, P) = \begin{cases} (1.0, 0, 0, 0, 2.0) & \text{for } r < 0.5 \\ (1.0, 0, 0, 0, 1.0) & \text{else.} \end{cases} \quad (49)$$

We show the numerical solution (200^3 particles, cubic lattice; MI1) at time $t = 0.2$ in Fig. 14. Again, the SPH result is in very good agreement with the (higher resolved) reference solution, only the

inner density plateau is somewhat smeared out, and there is a small wiggle at the contact discontinuity. This could be cured, for example, by applying a larger amount of conductivity (keep in mind we only use a small value, $\alpha_u = 0.05$). In this test all three the SPH formulations perform well, the matrix-inversion versions capture the central density plateau better and show a smaller overshoot than the kernel-gradient version, see Fig. 15. Note that in both circular blast wave problems the spherical symmetry is very well preserved, despite the initial particle setup on a cubic lattice.

3.4.6 Noh test

Next we consider the very challenging 3D Noh implosion test (Noh 1987) which has the reputation as a "code breaker", since a number of established methods are not able to handle this test without breaking or simply producing wrong results (Liska & Wendroff 2003). The test is performed with a polytropic exponent of $\Gamma = 5/3$ and with initial conditions $[\rho_0, v_0^i, P_0] = [1, -\hat{r}_a^i, 10^{-10}]$, where \hat{r}_a^i is the i -component of the radial unit vector of particle a . This corresponds to the spherical inflow to a point and results in a self-similar shock moving outwards at a velocity $v_s = 1/3$. The shocked region ($r < v_s t$) has density $\rho_s = \rho_0[(\Gamma + 1)/(\Gamma - 1)]^3$. The pre-shock flow ($r > v_s t$) undergoes shock-less compression according to $\rho(r, t) = \rho_0(1 - v_0 t/r)^2$.

The test is challenging for two reasons. First, the initial conditions contain an unresolved point of convergence that gives rise to the well-known "wall heating problem" where the thermal energy overshoots at the origin while the density undershoots in order to strive for the correct pressure. This phenomenon lead to the original suggestion to apply an artificial conductivity (Noh 1987) to alleviate the problem. The second difficulty is that the adiabatic pre-shock compression should not produce entropy which is a serious challenge for most artificial viscosity schemes.

We setup this challenging test similar to Sedov test case: we distribute 2.3×10^7 particles according to a Centroidal Voronoi Tessellation (Du et al. 1999) and subsequently perform 1000 correction sweeps according to Eq. (40). We show in Fig. 16 the density for this test (for the MII equation set; the other equation sets give very similar results), ρ , v and P are shown in Fig. 17 compared with the exact solution⁷. At the centre the "wall-heating problem" with a substantial density undershoot is encountered and the pressure is about 4% below the theoretical value. Nevertheless, compared to most existing methods MAGMA2 performs rather well in this challenging test. The wall heating effect could be alleviated by employing larger α_u -values. The PHANTOM code (Price et al. 2018), for example, uses $\alpha_u = 1$ and the authors report to have not found serious artefacts from this large value. However, given the somewhat pathological initial conditions with its unresolved point of convergence, we are not excessively worried about the encountered wall-heating problem (that is shared by most other methods) and do not see this as a strong incentive to increase the dissipation parameter α_u beyond the chosen, low value.

3.5 Instabilities

3.5.1 Kelvin-Helmholtz Instability

Kelvin-Helmholtz (KH) instabilities occur in shear flows with a perturbed interface. They play an important role in astrophysics and

occur in a broad range of environments, e.g. in mixing processes in novae (Casanova et al. 2011), amplification of magnetic fields in neutron star mergers (Price & Rosswog 2006; Giacomazzo et al. 2015; Kiuchi et al. 2015) or planetary atmospheres (Johnson et al. 2014), to name just a few. Traditional versions of SPH, however, have been shown to struggle with weakly triggered KH-instabilities (Agertz et al. 2007; McNally et al. 2012). We focus here on a test setup in which traditional SPH has been shown to fail, even at rather high resolution in 2D, see McNally et al. (2012). We follow the latter paper in setting up the test with the only difference that we use our full 3D code to perform the test in quasi-2D. To this end we set up a thin 3D slice with $N \times N \times 20$ particles (referred to as " N^2 "), for simplicity initially placed on a cubic lattice. Periodic boundary conditions are obtained by placing appropriate particle copies outside of the "core" volume. The test is initialised as:

$$\rho(y) = \begin{cases} \rho_1 - \rho_m e^{(y-0.25)/\Delta} & \text{for } 0.00 \leq y < 0.25 \\ \rho_2 + \rho_m e^{(0.25-y)/\Delta} & \text{for } 0.25 \leq y < 0.50 \\ \rho_2 + \rho_m e^{(y-0.75)/\Delta} & \text{for } 0.50 \leq y < 0.75 \\ \rho_1 - \rho_m e^{(0.75-y)/\Delta} & \text{for } 0.75 \leq y < 1.00 \end{cases} \quad (50)$$

where $\rho_1 = 1$, $\rho_2 = 2$, $\rho_m = (\rho_1 - \rho_2)/2$ and $\Delta = 0.025$. The velocity is set up as

$$v_x(y) = \begin{cases} v_1 - v_m e^{(y-0.25)/\Delta} & \text{for } 0.00 \leq y < 0.25 \\ v_2 + v_m e^{(0.25-y)/\Delta} & \text{for } 0.25 \leq y < 0.50 \\ v_2 + v_m e^{(y-0.75)/\Delta} & \text{for } 0.50 \leq y < 0.75 \\ v_1 - v_m e^{(0.75-y)/\Delta} & \text{for } 0.75 \leq y < 1.00 \end{cases} \quad (51)$$

with $v_1 = 0.5$, $v_2 = -0.5$, $v_m = (v_1 - v_2)/2$ and a small velocity perturbation in y -direction is introduced as $v_y = 0.01 \sin(2\pi x/\lambda)$ with the perturbation wave length $\lambda = 0.5$. In the linear regime, the instability grows on a characteristic time scale of

$$\tau_{\text{KH}} = \frac{(\rho_1 + \rho_2)\lambda}{\sqrt{\rho_1 \rho_2} |v_1 - v_2|}, \quad (52)$$

with $\tau_{\text{KH}} \approx 1.06$ for the chosen parameters. The test is performed with a polytropic equation of state with exponent $\Gamma = 5/3$.

We show in Fig. 18 the evolution of the instability at times $t = 1.5, 2.0$ and 2.5 for resolutions of 128^2 , 256^2 and 512^2 particles and the MII formulation. All cases grow at very similar rates and produce the characteristic "Kelvin-Helmholtz billows", even at the lowest resolution. For comparison, traditional SPH implementations struggle with this only weakly triggered instability ($v_y = 0.01$), see, for example, Fig. 9 of McNally et al. (2012), where even at a resolution 512^2 particles the instability hardly grows (for the cubic spline kernel, label "Ne512") or much too slowly (for the quintic spline kernel, label "No512"). In Fig. 19 we show the mode growth (calculated exactly as in McNally et al. (2012)) for all our cases compared to a high-resolution reference solution (4096^2 cells) obtained by the PENCIL code (Brandenburg & Dobler 2002). Even our low-resolution case with 128^2 particles is very close to the reference solution, the growth rates of the higher resolution cases are hard to distinguish from the reference solution.

It is instructive to repeat this test (at fixed resolution of 256^2 particles) and each time vary one of the choices we have made, starting the MII formulation with default choices as baseline. Density snapshots of these experiments are shown in Fig. 20, the corresponding growth rates are shown in Fig. 21. As first line in Fig. 20 we show the results obtained with our MII default choices. For the results in line two we used the same choices, but only linear reconstruction; line three used no reconstruction at all; line four applied the default choices, but used kernel gradients (instead of matrix-inversion gradients) and, finally, line five used the cubic spline kernel with 50

⁷ <http://cococubed.asu.edu>

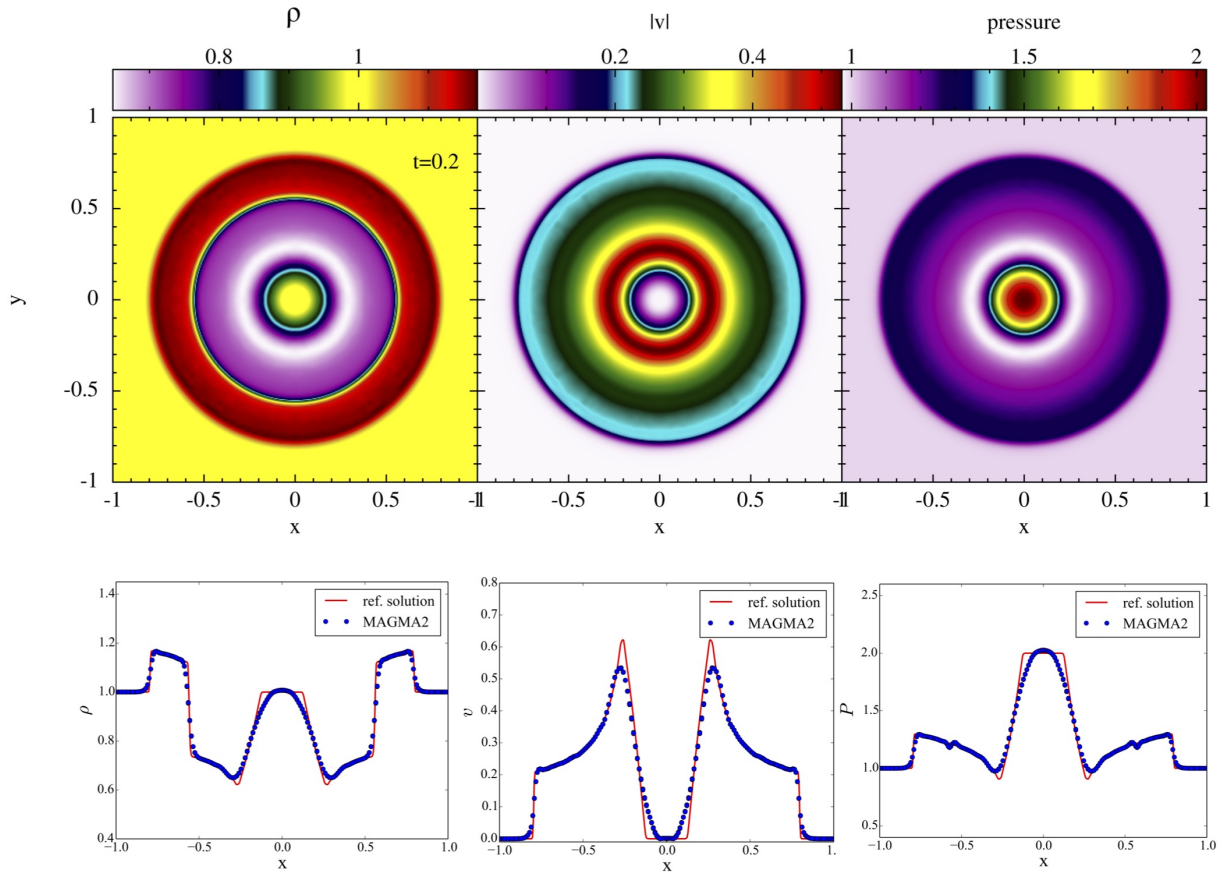


Figure 14. Circular blast wave problem 2 in 3D at $t = 0.2$ (200^3 particles). Upper row: MAGMA2 result for density, $|v|$ and pressure. Lower row: corresponding quantities from MAGMA2 results compared with a reference solution (red line) obtained by the Eulerian weighted average flux method (400^3 grid cells; (Toro 1999)).

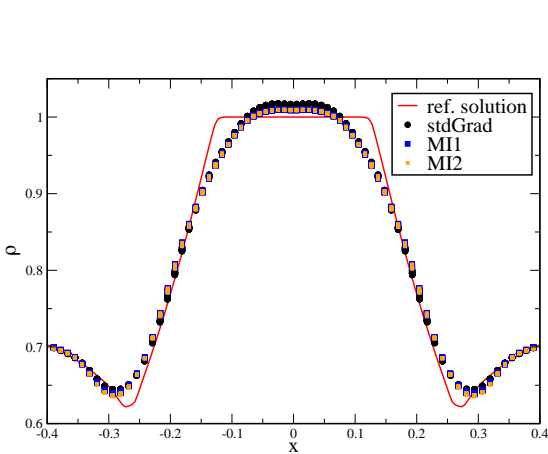


Figure 15. Zoom into the central density region of the circular blast wave problem 2 for the three different SPH formulations (stdGrad, MI1 and MI2; 200^3 particles). The reference solution (red line) has been obtained by the Eulerian weighted average flux method (Toro 1999) with 400^3 grid cells.

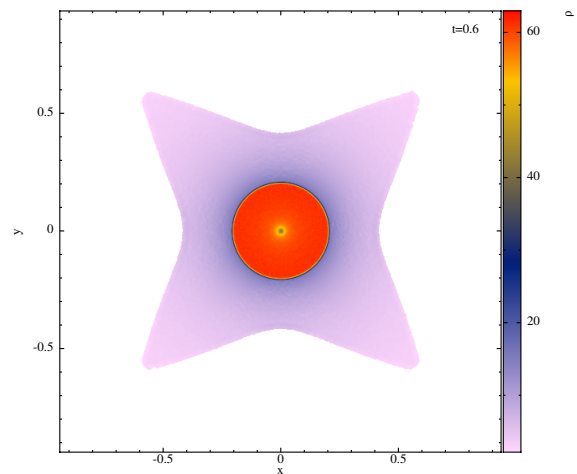


Figure 16. Result of the challenging 3D Noh implosion test (with the MI1 equation set). Shown is the density distribution in the XY-plane at $t = 0.6$.

neighbours rather than the WC6 kernel with 300 neighbours. The reconstruction, which substantially reduces the net dissipation, has clearly the largest impact in this test. The differences between the quadratic and linear reconstruction are only moderate, the interfaces between the high and low density parts remain sharper in

the former case (this is confirmed by running the simulations for longer). Not using any reconstruction at all, i.e. applying the common SPH approach of using the velocity differences at the particle positions, suppresses the growth of the instability all together, see the magenta diamonds in Fig. 21. Note, however, that this could also be improved by applying time-dependent dissipation schemes

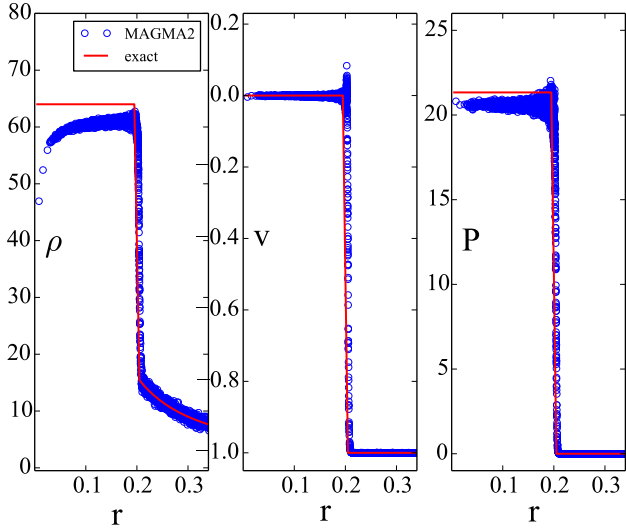


Figure 17. Result of the challenging 3D Noh implosion test (MI1), the exact solution is shown as solid red line.

(Morris & Monaghan 1997; Rosswog et al. 2000; Cullen & Dehnen 2010; Rosswog 2015a; Price et al. 2018; Rosswog 2020). The version with standard gradients also shows healthy growth, albeit at a somewhat lower rate and at $t = 1.5$ the edges of the high-density region are rather noisy. Although the cubic spline kernel has been found to be inferior to higher order kernels (Rosswog 2015a; Tricco 2019) it delivers in this test (together with matrix-gradients and large dissipation, but velocity reconstruction) satisfactory results. With all other options being the same, we see a small difference in the growth rate between the two different symmetrisations of the matrix-inversion formulations, but MI2 is even closer to the high-resolution reference solution (open circles vs filled circles in Fig. 21).

Obviously, the growth rates are in good agreement with the reference solution, even at very low resolution and one may wonder how important the thermal conductivity is for this result. To find out, we perform the following experiment. We set up 128^2 particles with the APM⁸, Sec. 3.1, and run for each simulation the test once with default parameters and once with default parameters, but without conductivity. As can be seen in Fig. 22, the impact of conductivity is rather small and it seems that (apart from the reconstruction) the largest impact is made by the gradient accuracy: both matrix inversion formulations (columns 3 to 6) show even at this low resolution a healthy growth, rather independent of conductivity, while the standard gradient version struggles and only grows with some noticeable delay, both with and without conductivity (columns 1 and 2).

3.5.2 Rayleigh-Taylor instability

The Rayleigh-Taylor instability is a standard probe of the subsonic growth of a small perturbation. In its simplest form, a layer of density ρ_t rests on top of a layer with density $\rho_b < \rho_t$ in a constant acceleration field, e.g. due to gravity. While the denser fluid sinks down, it develops a characteristic, "mushroom-like" pattern. Simulations with traditional SPH implementations have shown only

retarded growth or even a complete suppression of the instability (Abel 2011; Saitoh & Makino 2013).

As before, we adopt a quasi-2D setup and use the full 3D code for the evolution. We place the particles on a CL in the XY-domain $[-0.25, 0.25] \times [0, 1]$ and we use 8 layers of particles in the Z-direction. Similar to Frontiere et al. (2017) we use $\rho_t = 2$, $\rho_b = 1$, a constant acceleration $\vec{g} = -0.5\hat{e}_y$ and

$$\rho(y) = \rho_b + \frac{\rho_t - \rho_b}{1 + \exp[-(y - y_t)/\Delta]} \quad (53)$$

with transition width $\Delta = 0.025$ and transition coordinate $y_t = 0.5$. We apply a small velocity perturbation to the interface

$$v_y(x, y) = \delta v_{y,0} [1 + \cos(8\pi x)] [1 + \cos(5\pi(y - y_t))] \quad (54)$$

for y in $[0.3, 0.7]$ with an initial amplitude $\delta v_{y,0} = 0.025$, and use a polytropic equation of state with exponent $\Gamma = 1.4$. The equilibrium pressure profile is given by

$$P(y) = P_0 - g\rho(y)[y - y_t] \quad (55)$$

with $P_0 = \rho_t/\Gamma$, so that the sound speed is near unity in the transition region. To enforce boundary conditions we add 10 rows of extra particles ($y > 1$ and $y < 0$) that we "freeze" at the initial conditions and we use periodic boundary conditions elsewhere.

We show in Fig. 23 the results of several simulations at a time of $t = 4$. The first panel shows the result for a simulation that uses the standard SPH approach with kernel gradients and a XY-resolution of 128×256 particles which overall performs reasonable well. The second to fourth panel shows the results for everything else being the same (MI1 formulation), but using matrix-inversion kernels instead. This version delivers finer resolved/less diffusive density structures and a larger plunge depth. With increasing resolution the density transitions become sharper and more substructure appears, but the plunge depth remains the same.

A comparison between the MI1 and MI2 formulation, see Fig. 24, demonstrates that the latter shows a larger amount of mixing, consistent with the results from Sec. 3.3.

3.6 Complex shocks with vorticity creation

A set of challenging 2D benchmark tests has been suggested by Schulz-Rinne (1993). They are constructed in such a way that four constant states meet at one corner and the initial values are chosen so that one elementary wave, either a shock, a rarefaction or a contact discontinuity appears at each interface. During the subsequent evolution complex wave patterns emerge for which no exact solutions are known. These tests are considered challenging benchmarks for multi-dimensional hydrodynamics codes (Schulz-Rinne 1993; Lax & Liu 1998; Kurganov & Tadmor 2002; Liska & Wendroff 2003). Such tests are rarely shown for SPH codes, in fact, we are only aware of the work by Puri & Ramachandran (2014) who show results for one such shock test in a study of Godunov SPH with approximate Riemann solvers.

Here we investigate six such configurations. Since our code is intrinsically 3D, we simulate, as before, a slice thick enough so that the midplane is unaffected by edge effects (we use 10 particle layers in Z-direction). We use 660×660 particles in the XY-plane arranged on a hexagonal lattice between $[x_c - 0.5, x_c + 0.5] \times [y_c - 0.5, y_c + 0.5]$, (x_c, y_c) being the contact point of the quadrants, and we use a polytropic exponent $\Gamma = 1.4$ in all of the tests. We refer to these Schulz-Rinne type problems as SR1 - SR6 and give their initial parameters for each quadrant in Tab. 1. These test problems correspond to configuration 3, 4, 5, 6, 11 and 12 in the labelling

⁸ We hardly see a difference for a grid setup.

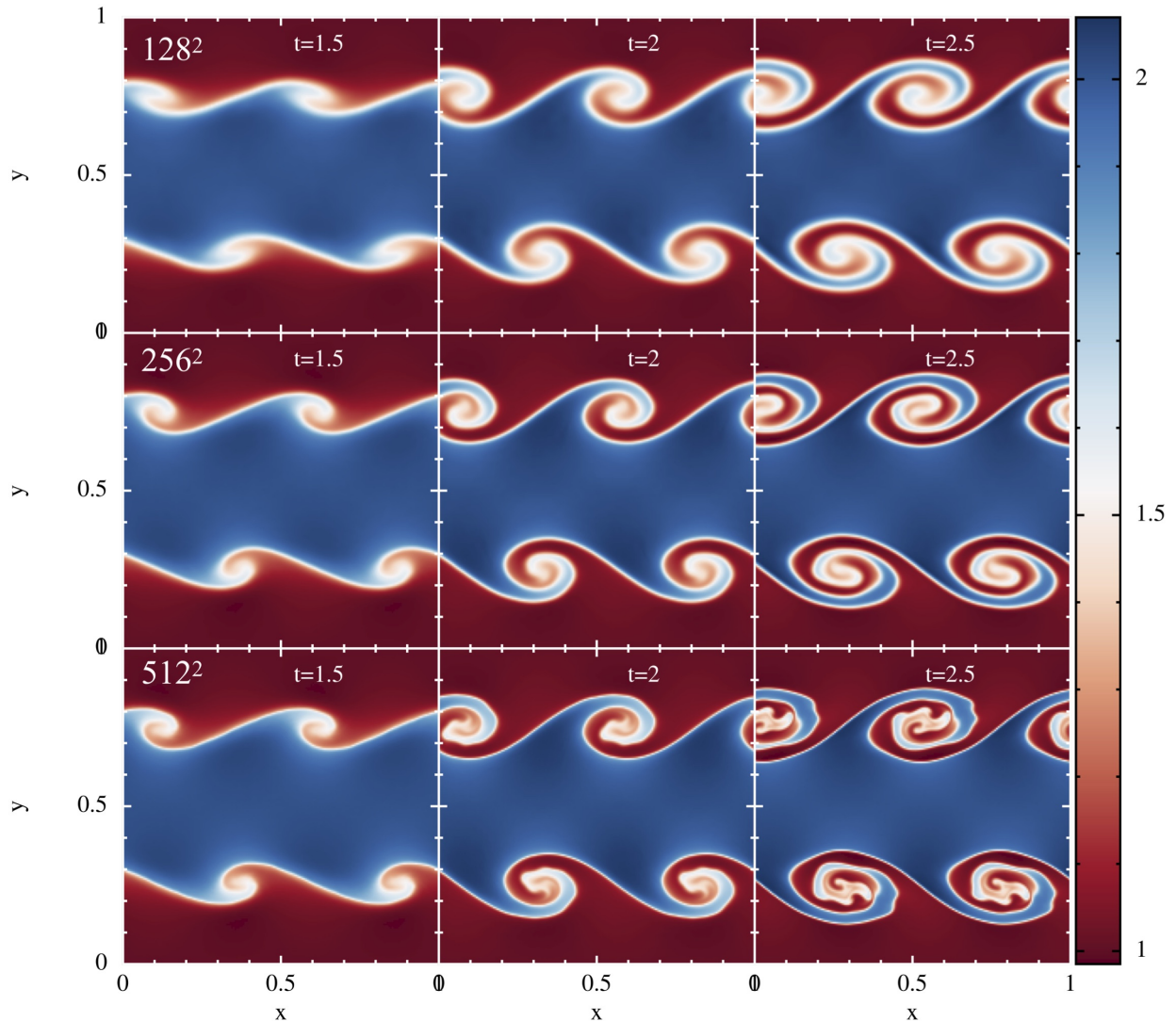


Figure 18. Density evolution for weakly triggered Kelvin-Helmholtz instability at $(128 \times 128 \times 8)$, $(256 \times 256 \times 8)$ and $(512 \times 512 \times 8)$ particles resolution.

convention of Kurganov & Tadmor (2002). Our results (M11) are shown in Fig. 25.

Test SR1 is the only one of the Schulz-Rinne tests that has to our knowledge been tackled with (Godunov-)SPH (Puri & Ramachandran 2014). Their results show that existing SPH implementations struggle to resolve the mushroom-like structure along the diagonal (roughly at $x \approx y \approx 0.2$ in our figure, upper left panel) and depending on the chosen approximate Riemann solver serious artefacts appear. Our results, in contrast, show crisp transitions between the different regions, well developed “mushrooms” and they look overall similar to those found with established Eulerian methods, see e.g. Liska & Wendroff (2003), their Fig.4.1. In test SR2 straight 1D shocks separating constant states and two curved shocks bordering a lens-shaped high-density/-pressure region occur. The result should be symmetric with respect to the lens axis and the MAGMA2 results do not show any noticeable deviation from perfect symmetry. Test SR3 yields a lense-shaped central region with two vortex structures occurring at the upper left and lower right part of the shown domain. Again, our result at $t = 0.23$ closely resembles those in the literature, e.g. Lax & Liu (1998), their Fig.5. This is

also true for the remaining tests, SR 4 can be compared, e.g. with Fig. 4.1 in Liska & Wendroff (2003), SR 5 with Fig. 11 in Lax & Liu (1998) and SR6 with Fig. 4.4 in Liska & Wendroff (2003). Note that all tests show a high (though not perfect) degree of symmetry which –with freely moving particles– is not actively enforced. Overall, the tests are in very good agreement with the Eulerian results found in the literature (Lax & Liu 1998; Liska & Wendroff 2003) and they look crisp and noise free. Note in particular the appearance of mushroom-like structures (in panels 1, 5 and 6) which are usually considered a challenge for SPH-methods. Some of the weak straight lines in the panels, however, are considered spurious. But these artefacts are shared by the majority of methods found in the literature.

3.7 Astrophysical applications

In this last section we show tests that are close to astrophysical applications. The purpose of these tests is to demonstrate the performance of the dissipation scheme, measure the numerical conservation in a relevant example and to show robustness and geomet-

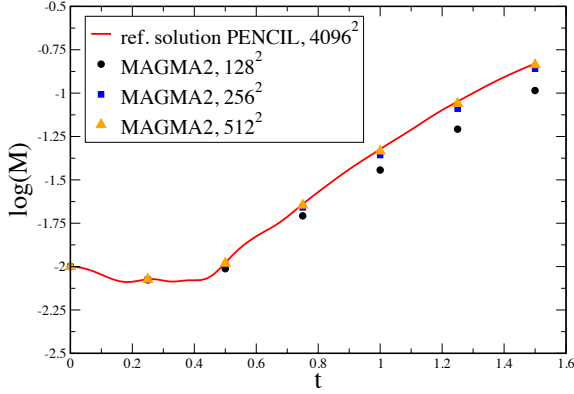


Figure 19. Resolution dependence of the Kelvin-Helmholtz mode amplitude growth (MI1). As reference solution (solid, red) we use a simulation with the Pencil Code at a resolution of 4096^2 . Note that all cases show a growth close to the reference solution, even at the lowest resolution (128^2 particles). For comparison, traditional SPH simulations struggle with this only weakly triggered test, even at substantially higher resolution of 512^2 (McNally et al. 2012).

ric flexibility. We did not find noteworthy differences between different SPH-formulations in these tests and, unless explicitly stated otherwise, we show the MI1-results.

3.7.1 Oscillating White Dwarf

As another experiment, we take a relaxed $\Gamma = 5/3$ -polytropic star that represents a model for a $0.3 M_{\odot}$ WD. We use only 10K SPH particles and provide them with a radial velocity $\vec{v}_a = v_0 \vec{r}_a$, where we choose $v_0 = 0.02$. As before, all tests use constant dissipation parameters of $\alpha = 1$. To avoid dissipation from other sources, we run these tests with low tolerance for the tree accuracy ($\Theta = 0.1$) and a time integration prefactor $C = 0.1$. The evolution of the oscillations in the gravitational energy are shown Fig. 26. As blue line we show the standard SPH-approach, i.e. without velocity reconstruction, the red line shows our default choice of methods and parameters and the black, open circles show the result for the default choices, but with $\alpha_u = 0$. Consistent with the experiments in the Kelvin-Helmholtz instability test, see Fig. 20, we find a massive suppression of unwanted dissipation when velocity reconstruction is employed. As intended, artificial conductivity does not switch on in this test problem, the results with $\alpha_u = 0$ lie nearly exactly on top of the $\alpha_u = 0.05$ (default).

3.7.2 Collapse of isothermal sphere

The collapse of an initially isothermal cloud is another frequently performed complex code test (Evrard 1988; Hernquist & Katz 1989; Steinmetz & Müller 1993; Dave et al. 1997; Springel et al. 2001; Wadsley et al. 2004; Cabezón et al. 2017; Price et al. 2018) that tests for the coupling of gravity and hydrodynamics. The test starts with a gas cloud at rest that collapses under its own gravitational, then forms a shock, bounces back with a shock wave moving outward until the system settles into a virial equilibrium. This benchmark tests the transformation between different forms of energy: initially mostly gravitational, then kinetic and finally thermal.

Table 1. Initial data for the Schulz-Rinne-type 2D Riemann problems

SR1; contact point: (0.3, 0.3)				
variable	NW	NE	SW	SE
ρ	0.5323	1.5000	0.1380	0.5323
v_x	1.2060	0.0000	1.2060	0.0000
v_y	0.0000	0.0000	1.2060	1.2060
P	0.3000	1.5000	0.0290	0.3000
SR2; contact point: (-0.15, -0.15)				
variable	NW	NE	SW	SE
ρ	0.5065	1.1000	1.1000	0.5065
v_x	0.8939	0.0000	0.8939	0.0000
v_y	0.0000	0.0000	0.8939	0.8939
P	0.3500	1.1000	1.1000	0.3500
SR3; contact point: (0.0, 0.0)				
variable	NW	NE	SW	SE
ρ	2.0000	1.0000	1.0000	3.0000
v_x	-0.7500	-0.7500	0.7500	0.7500
v_y	0.5000	-0.5000	0.5000	-0.5000
P	1.0000	1.0000	1.0000	1.0000
SR4; contact point: (0.0, 0.0)				
variable	NW	NE	SW	SE
ρ	2.0000	1.0000	1.0000	3.0000
v_x	0.7500	0.7500	-0.7500	-0.7500
v_y	0.5000	-0.5000	0.5000	-0.5000
P	1.0000	1.0000	1.0000	1.0000
SR5; contact point: (0.0, 0.0)				
variable	NW	NE	SW	SE
ρ	0.5313	1.0000	0.8000	0.5313
v_x	0.8276	0.1000	0.1000	0.1000
v_y	0.0000	0.0000	0.0000	0.7276
P	0.4000	1.0000	0.4000	0.4000
SR6; contact point: (0.0, 0.0)				
variable	NW	NE	SW	SE
ρ	1.0000	0.5313	0.8000	1.0000
v_x	0.7276	0.0000	0.0000	0.0000
v_y	0.0000	0.0000	0.0000	0.7262
P	1.0000	0.4000	1.0000	1.0000

We prepare the setup according to the parameters of Evrard (1988) with

$$\rho(r) = \frac{M(R)}{2\pi R^2 r}, \quad (56)$$

where the initial cloud radius is $R = 1$ and the mass $M = 1$. Similar to other tests, we set up 10^6 SPH particles according to a centroidal Voronoi tessellation (Du et al. 1999) and subsequently perform 5000 sweeps according to Eq. (40) to further improve the initial particle distribution. We then assign masses so that the initial density profile is reproduced, set the internal energy to $u = 0.05GM/R$ and use a polytropic exponent of $\Gamma = 5/3$.

As a first step, we compare the MAGMA2 result with "standard SPH choices", specifically a) a cubic spline kernel with 50 neighbour

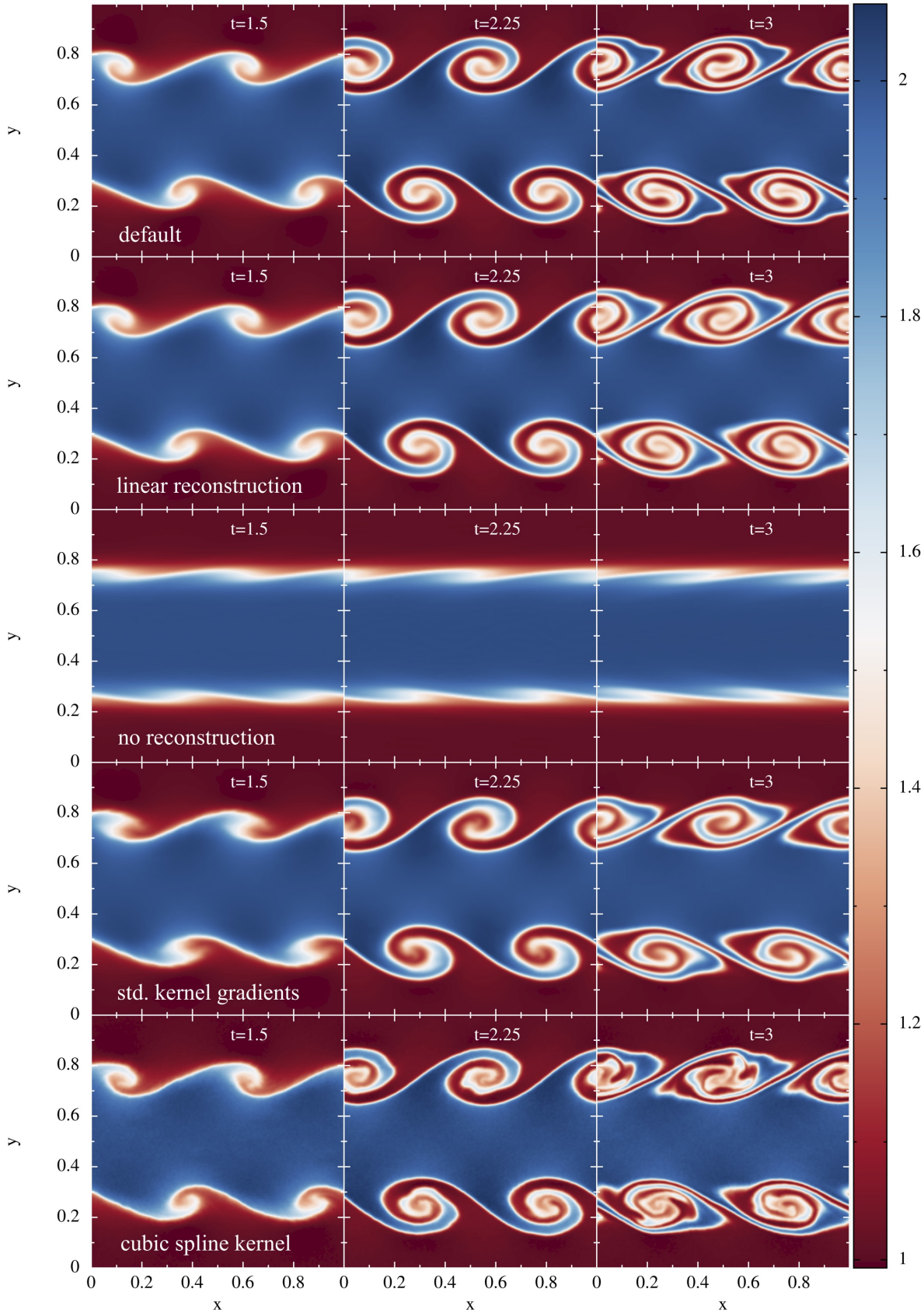


Figure 20. 3D Kelvin-Helmholtz test ($256 \times 256 \times 20$ particles) where we explore the impact of different methodological choices. The first row shows our default choice with matrix-inversion gradients (MI1), artificial dissipation that uses a slope-limited, quadratic velocity reconstruction and the high-order Wendland kernel. Second row: as row 1, but only using linear reconstruction. Third row: as default, but no reconstruction, just using the velocity differences between particles; this is the conventional way of implementing artificial viscosity in SPH; Fourth row: as default, but using kernel gradients; Fifth row: as default, but using the cubic spline kernel.

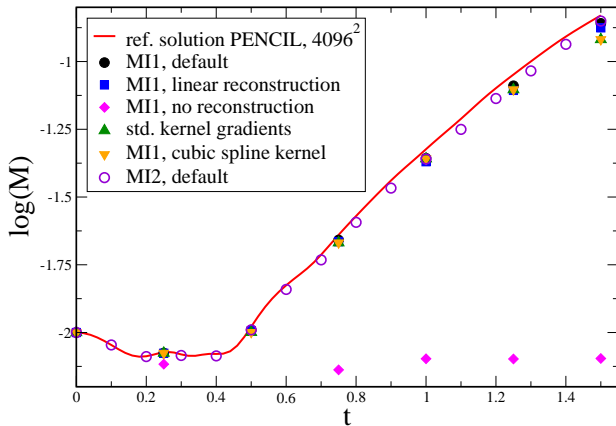


Figure 21. Growth of the Kelvin-Helmholtz mode amplitude for the 256^2 -case where we vary methodological choices as in Fig. 20. The results for the MI1 default choices are shown as black circles, the results with only linear reconstruction (blue square) grow at a similar rate, but slightly slower. Both the case with standard kernel gradients (green triangles) and the one using the cubic spline kernel (orange triangles) grow somewhat slower. The largest impact in this test, however, has the velocity reconstruction: if it is not applied and the standard SPH prescription is applied instead, the instability is suppressed (magenta diamonds). The symmetrisation in the matrix inversion formulation does make a small difference in the growth rate, with MI2 growing slightly faster.

particles, b) constant dissipation ($\alpha = 1, \beta = 2$) without reconstruction and c) standard kernel gradients to calculate derivatives. Note that this is different from what we had abbreviated before as “std-Grad”: the latter uses kernel gradients, but all the other benefits of MAGMA2. The results of the MI2 formulation (with all default choices) and the “standard SPH choices” for a low resolution case with 10^5 SPH particles is shown in Fig. 27 at $t = 0.77$. Compared to the reference solution (Steinmetz & Müller 1993), our low-resolution MI2 result shows a velocity overshoot at the shock (left panel), but otherwise agrees well. The “standard SPH choice” version, in contrast, shows a fair amount of spurious entropy production (middle panel), so that the shock is broadly smeared out (left and right panel) and actually sitting at too large a radius.

Thus, the MAGMA2 results are a major improvement over traditional SPH choices. Among our different SPH variants we only find very minor differences in this test. We show a case with 10^6 SPH particles, prepared as before, in Fig. 28 together with the reference solution (Steinmetz & Müller 1993). Note that all particles are plotted in the figure. All three formulations are nearly perfectly spherically symmetric and agree very well with the reference solution. Only at the shock front there is some velocity overshoot.

3.7.3 Collision between two main sequence stars

In this test we simulate a collision between two main sequence stars. The aim is, on the one hand, to demonstrate the robustness and usefulness for the simulation of violent astrophysical events and, on the other hand, to measure how accurately matrix-inversion formulations numerically conserve physically conserved quantities for typical simulation parameters (such as the tree opening criterion and time integration prefactor.) For the simulation we choose two

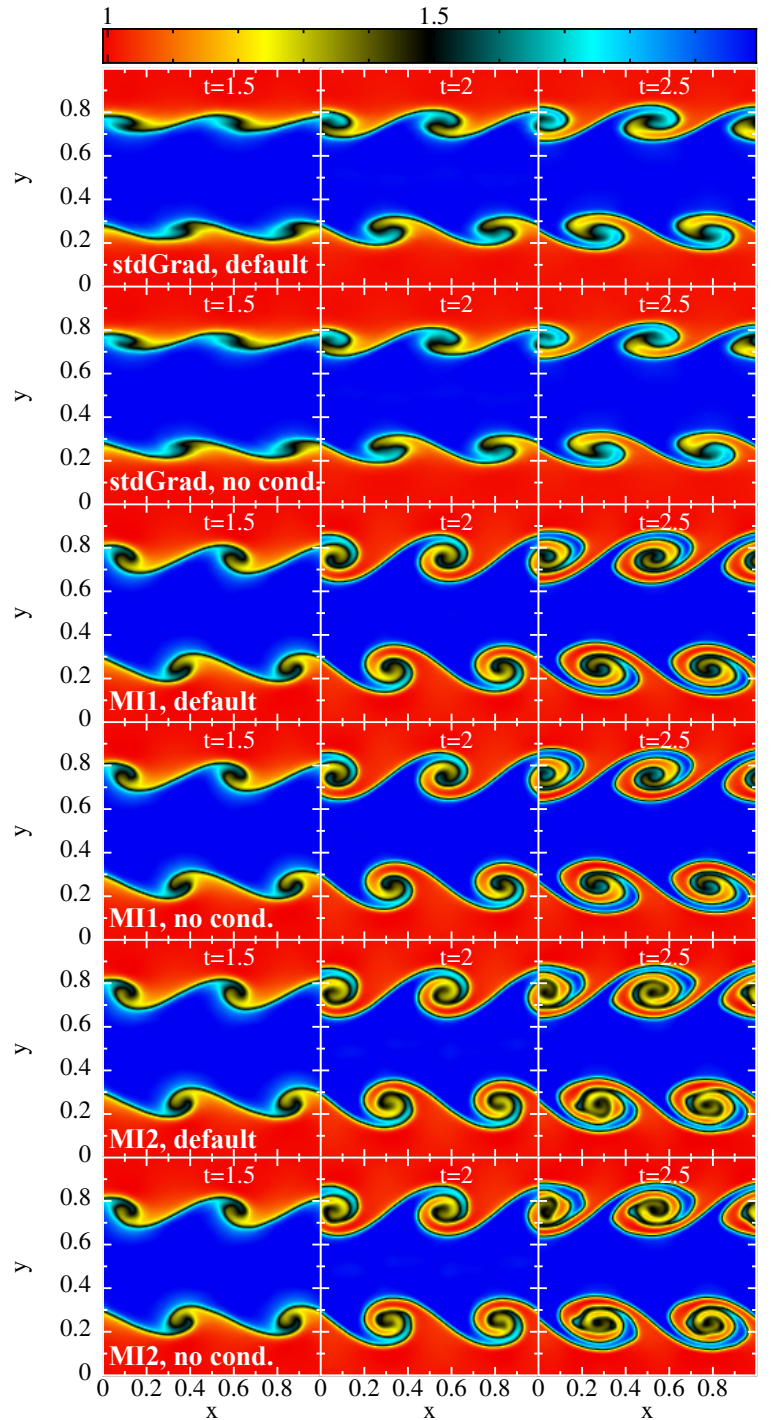


Figure 22. Low resolution (“ 128^2 particles”) test of the importance of thermal conductivity for our different SPH formulations in a Kelvin-Helmholtz problem: standard kernel gradients (“stdGrad”; rows 1 and 2), matrix inversion formulation 1 (“MI1”; rows 3 and 4) and matrix inversion formulation 2 (“MI2”; rows 5 and 6), each time once with conductivity and once without. For none of our SPH-variants does the conductivity play a major role, results are mostly determined by artificial viscosity (velocity reconstruction or not?) and the accuracy of the hydrodynamic gradients.

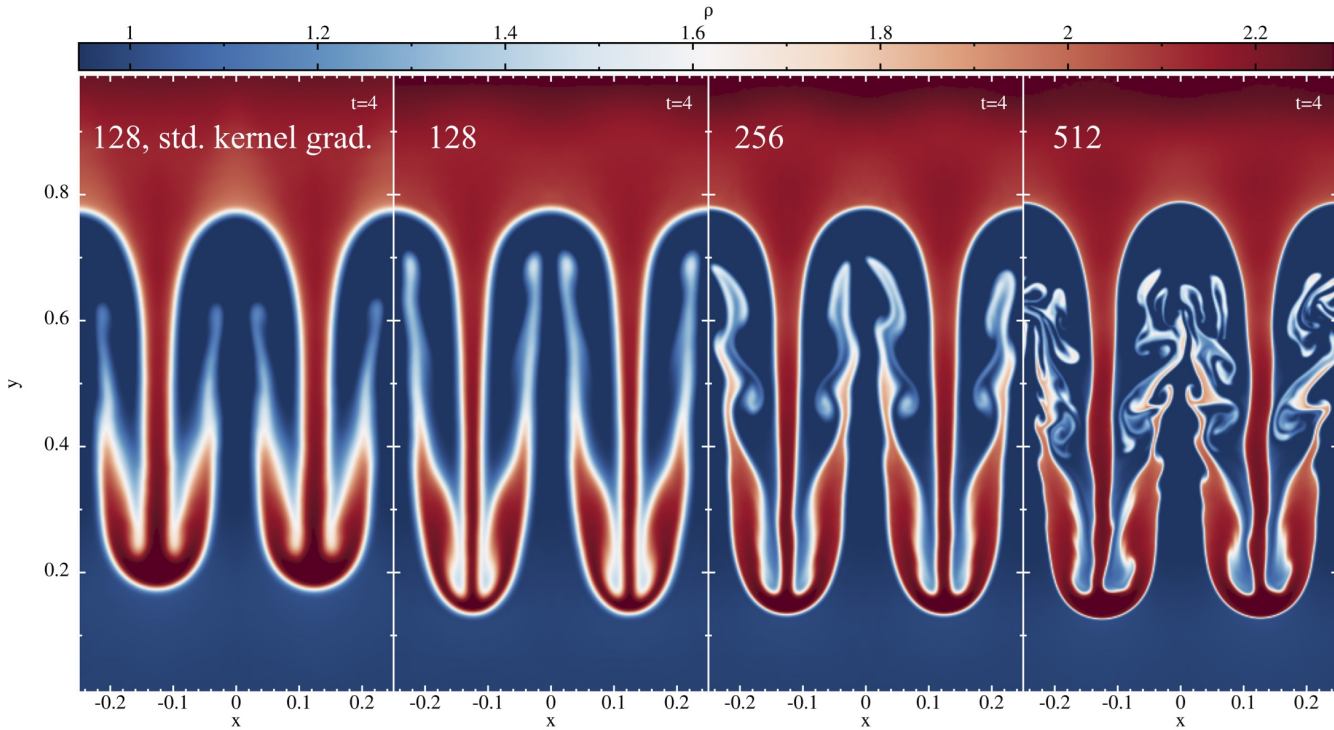


Figure 23. The first Rayleigh-Taylor test (first panel) uses kernel-gradients as is common practice in SPH (“128 × 256” particles), all other tests use our default choices of matrix-inversion gradients (“128 × 256”, “256 × 512” and “512 × 1026” particles). Panels 2-4 show the result of the MI1 formulation.

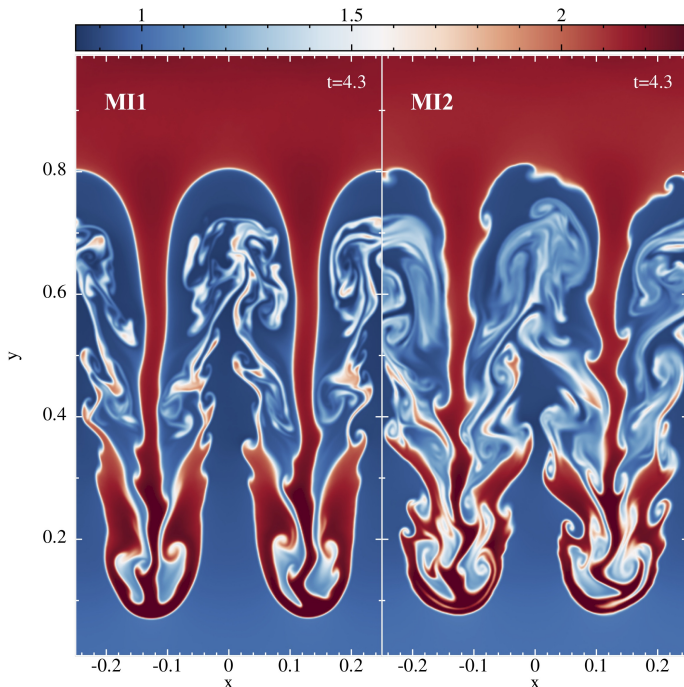


Figure 24. Comparison of a Rayleigh-Taylor test (density, 512^2) at $t = 4.3$ between the MI1 and MI2 formulation.

identical stars, each with a mass $M_* = 1M_\odot$ and a radius $R_* = R_\odot$, modelled as a $\Gamma = 5/3$ polytrope with 2×10^6 equal mass SPH particles. The stars approach each other on a parabolic orbit with an

impact strength

$$\beta \equiv \frac{2R_*}{R_{\text{peri}}} = 3. \quad (57)$$

We perform this simulation twice, once with the evolution equation set that uses kernel gradients (stdGrad; first row in Fig. 29) and once with the equation set that uses matrix-inversion based gradients (MI1; second row). During the first collision the stars become heavily shocked (see panels 1 and 4), vorticity is created and the stellar cores are substantially spun up (panels 2 and 5). During the subsequent evolution the stars fall back towards each other, thereby creating further shocks and vorticity (panels 3 and 6). For this test we find very similar results. We have performed these simulations with parameters that we would use for a practical simulation: $C = 0.2$ in Eq. (34) and a (rather tolerant) tree opening criterion $\Theta = 0.9$, see Gafton & Rosswog (2011) for a detailed description of the used recursive coordinate bisection (RCB) tree. The latter guarantees a fast evaluation of the gravitational forces, though at the price of sacrificing some accuracy. Despite this seemingly tolerant opening criterion, the conservation of both energy and angular momentum for both approaches are better than 0.4%, see Fig. 30, and could be easily further improved by choosing a stricter force criterion.

3.7.4 Tidal disruption of a white dwarf star

As another astrophysical test case we show a tidal disruption of a $0.5 M_\odot$ white dwarf star by a $1000 M_\odot$ black hole. Such encounters can lead to a tidal ignition and explosion of the white dwarf (Luminet & Pichon 1989; Rosswog et al. 2008, 2009) provided that the black hole is of “intermediate” mass (below $\approx 10^5 M_\odot$). We show a weak encounter with a “penetration factor” $\beta = R_t/R_p = 0.9$, where

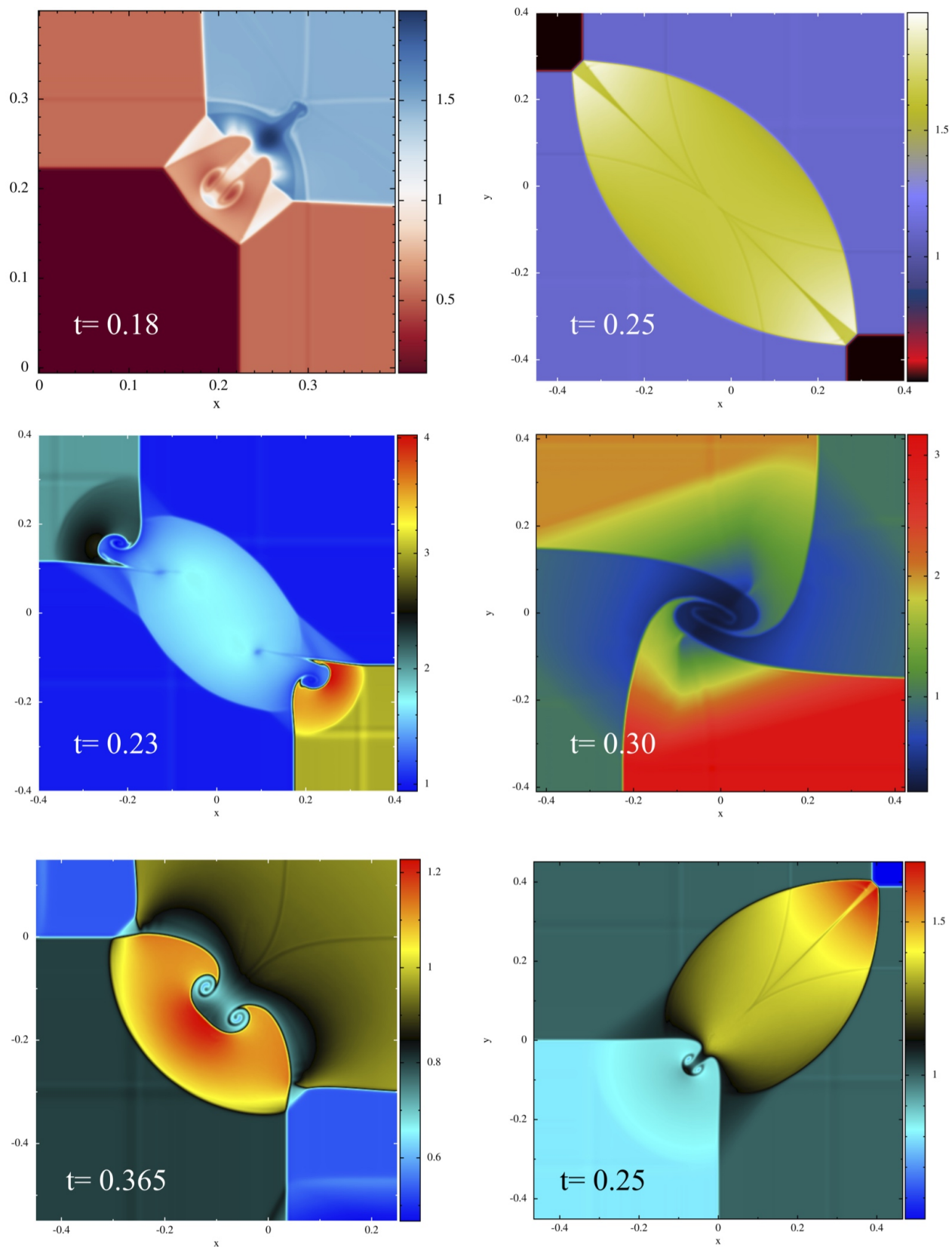


Figure 25. MAGMA2 solution (density) for the challenging Schulz-Rinne-type shock tests, see Tab. 1 for the initial conditions. For these tests no exact solutions are known, results need to be compared to other numerical schemes, see e.g. Lax and Liu (1998) or Liska and Wendroff (2003).

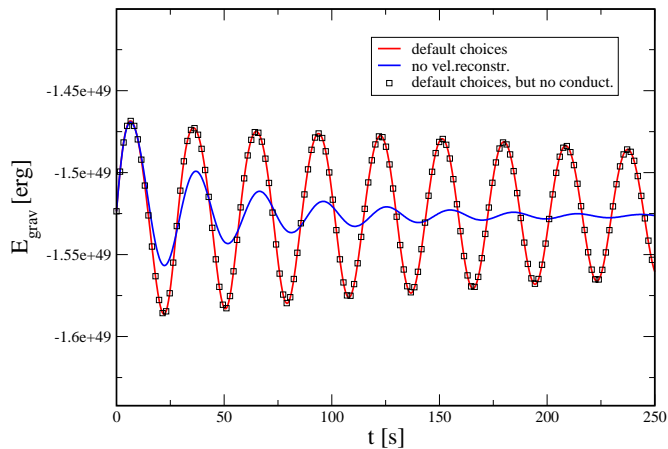


Figure 26. Gravitational energy of an oscillating polytropic white dwarf star with 10K particles. The blue line shows artificial viscosity applied as in standard SPH (without velocity reconstruction), the red line is our default choice for methods and parameters and the black squares are our default choices (only every fifth point shown), but without artificial conductivity, i.e. $\alpha_u = 0$.

$R_t = R_{\text{wd}}(M_{\text{bh}}/M_{\text{wd}})^{1/3}$ is the tidal radius inside of which a star is disrupted by the black hole’s tidal forces. The quantity R_p is the distance of closest approach (“pericentre distance”). We chose a value of $\beta < 1$, since this results in a partial disruption where the star is “nearly disrupted”, but while receding from the black hole its self-gravity overcomes the tidal pull again and a part of the tidal debris re-collapses into a self-gravitating core. Due to the highly elongated geometry and the small self-gravitating core such partial disruptions pose particular computational challenges.

We model the initial white dwarf as a polytrope with exponent $\Gamma = 5/3$ with 5×10^6 equal-mass SPH-particles. Since for the chosen parameters the pericenter distance is $R_p > 90GM_{\text{bh}}/c^2$, we can treat the black hole to excellent accuracy as a Newtonian point mass⁹. Initially the white dwarf is placed at a distance $r_0 = 6R_t$ which guarantees that the tidal acceleration is only a tiny perturbation ($\ll 1\%$) compared to self-gravity. In Fig. 31, left panel, we show the density in the orbital plane at $t = 9$ code units (1 code unit = 2.745 s), when the star is approaching the BH, at $t = 20$, after the star has just passed it, and at $t = 47$ when the central region has re-contracted into a self-gravitating core.

3.7.5 Double TDE

As a last astrophysical test we show the disruption of a stellar binary system of two Main Sequence stars by a supermassive black hole. Here, the main challenge comes from the widely varying geometry and the involved scales. Mandel & Levin (2015) studied tidal interactions of stellar binary systems with massive black holes and found that in a substantial fraction of cases both stars become disrupted. According to their estimate, close to 10% of all stellar

⁹ For relativistic encounters one can use MAGMA2 with either the accurate pseudo-potential of Tejeda & Rosswog (2013), or, even better, within the approach suggested in Tejeda et al. (2017).

tidal disruptions may be double disruption events.

We simulate here the disruption of a binary consisting of two massive stars of 67.01 and 36.8 M_{\odot} by a $M_{\text{bh}} = 10^6 M_{\odot}$ black hole (initial conditions kindly provided by Ilya Mandel). Fig. 32 shows four snapshots of this disruption (colour coded is column density). The first shows the stage ($t = 1.21$ hr) when the stars are approaching the black hole and the leading, more massive star is about to be disrupted. The second snapshot ($t = 2.77$ hr) shows the leading star being disrupted while the companion is approximately at pericentre. Snapshot three shows both disrupted stars receding from the black hole while in the last snapshot debris is fed in two narrow streams to the hole and an accretion disk is being assembled.

4 SUMMARY

In this paper we have presented the new Lagrangian hydrodynamics code MAGMA2, which benefits from a number enhancements compared to traditional SPH codes.

- MAGMA2 uses consistently high-order kernels which substantially reduce noise, but this comes at the price of large neighbour numbers. Our default choice is a Wendland C^6 kernel together with 300 neighbours in the kernel support of each particle.

- To produce entropy in shocks, our code employs artificial viscosity, but enhanced by techniques that are borrowed from finite volume methods. Instead of employing the velocity difference between two particles in the artificial viscosity terms (which is the common SPH practice), we use the difference of the *slope-limited, quadratically reconstructed velocities* at the inter-particle midpoint. All tests shown in this paper are performed with constant dissipation parameters ($\alpha = 1$ and $\beta = 2$) and even with such large parameters we find excellent results in benchmark tests. We have also implemented a new way to steer time-dependent dissipation by monitoring for each particle how well entropy is conserved. This allows to identify “troubled particles” that need their dissipation increased. This approach is discussed in detail in a separate publication (Rosswog 2020).

- Apart from a conventional SPH formulation (“stdGrad”) that calculates derivatives via kernel gradients, MAGMA2 also offers two additional SPH formulations that use much more accurate gradient estimates that are based on matrix inversion techniques (“MI1” and “MI2”), see Sec. 2.1. These two formulations only differ in the way the SPH equations are symmetrised. All three SPH versions are implemented with the above described kernels and artificial dissipation techniques.

- Self-gravity and neighbour search are implemented via a fast tree that tessellates space by means of a recursive coordinate bisection and that is described in detail in Gafton & Rosswog (2011).

- In Sec. 3.1 we suggest a new way to set up SPH initial conditions. SPH is known to perform best when equal-mass particles are used, but setting up geometrically complicated initial conditions with equal-mass particles is non-trivial. To address this problem we have introduced the *Artificial Pressure Method (APM)*, which is very much in the spirit of SPH. It starts from an initial distribution of equal mass SPH particles and compares the currently measured density with a desired density profile. Based on the local density errors it calculates an artificial pressure force that steers the SPH particles into positions where the deviations from the theoretical density profile are minimal.

We have scrutinised MAGMA2 in a large number of benchmark tests including smooth advection, a variety of shock and instability tests,

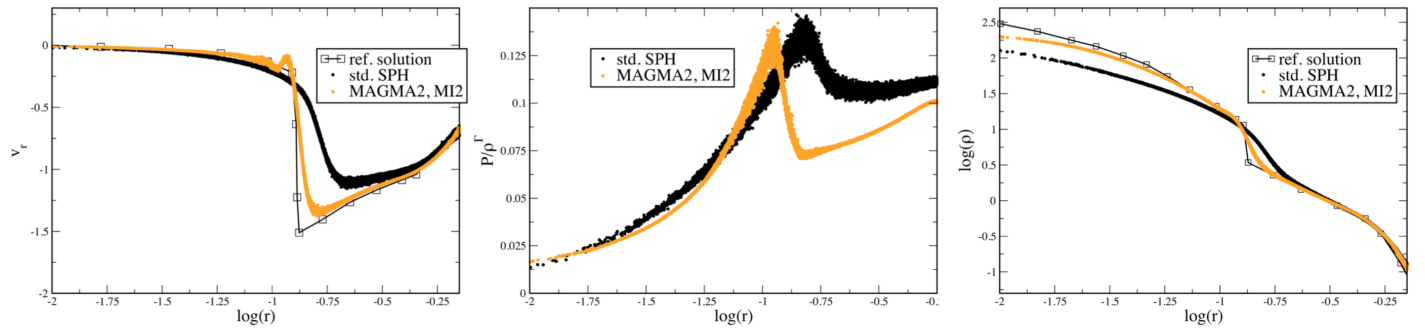


Figure 27. Results of Evrard’s isothermal cloud collapse (Evrard 1988) for a resolution of 10^5 particles. Shown are the results of “standard SPH” (no reconstruction, cubic spline kernel, kernel gradients; black) and one of MAGMA2’s formulations (MI2; orange) for velocity (left), entropy variable P/ρ^Γ (middle) and density (right) together with a 1D reference solution (Steinmetz & Müller 1993).

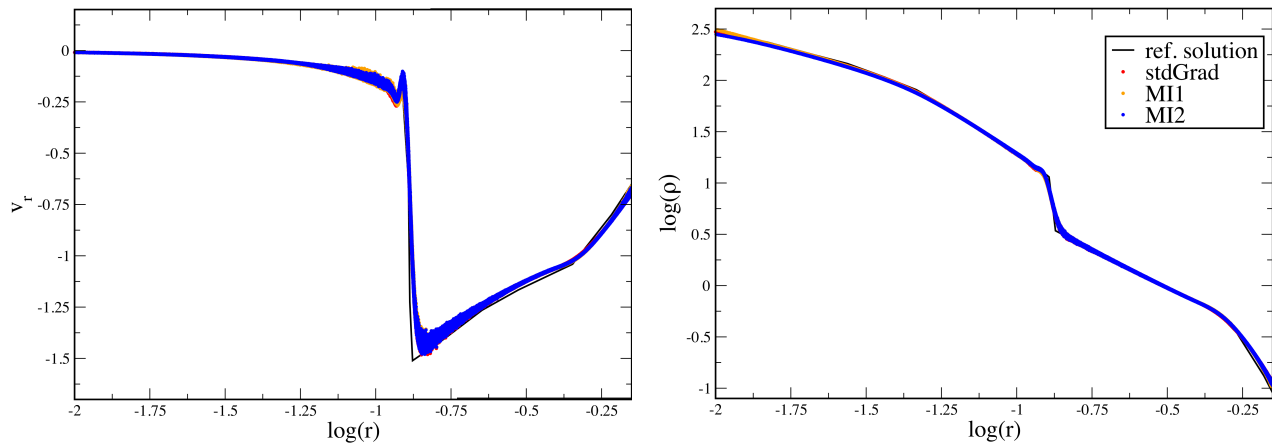


Figure 28. Results of Evrard’s isothermal cloud collapse (Evrard 1988). Shown are the results of all three SPH formulations (stdGrad, MI1, MI2; 10^6 particles, all are plotted) together with a reference solution (Steinmetz & Müller 1993). All our variants yield very similar results in this test.

vorticity creating Schulz-Rinne shocks (which are rarely shown in SPH publications) and a number of more astrophysical tests that demonstrate its robustness, versatility and excellent conservation properties. We find very good results in these benchmarks, also in tests that are traditionally considered a challenge for SPH codes. As expected, MAGMA2 is second order accurate in smooth flows, see Sec. 3.2 and it yields good results in shocks. The techniques borrowed from finite volume approaches (slope-limited reconstruction) in the artificial dissipation are a major improvement compared to the standard approach. For example, with reconstructed velocities, but large and constant artificial viscosity values MAGMA2 performs excellently in a Kelvin-Helmholtz test where SPH-approaches without such a reconstruction fail completely. Even the low resolution cases grow with rates very close to the (much higher resolved) reference solution. The effect of the quadratic reconstruction (as compared to a linear one) is small, though welcome. But it may be a valid choice to restrict oneself

to just linear reconstruction and to avoid the need of calculating second derivatives.

We have also introduced a set of matrix inversion SPH equations (MI2) with a rarely used symmetrisation in the particle indices. This symmetrisation (though different gradients, dissipation strategy, kernels etc.) has been successfully used the `GASOLINE2` code (Wadsley et al. 2017). While delivering in most tests very similar results to the other matrix inversion formulation (MI1), MI2 has some distinct advantages:

- it is substantially more sensitive to density variations and – with everything else being the same– achieves substantially better results in the Sedov explosion test than the other two formulations.
- in addition, it substantially reduces surface tension effects and therefore also has an advantage in instability tests compared to the other two SPH formulations.

The only slight disadvantage that we have noticed is that it is less

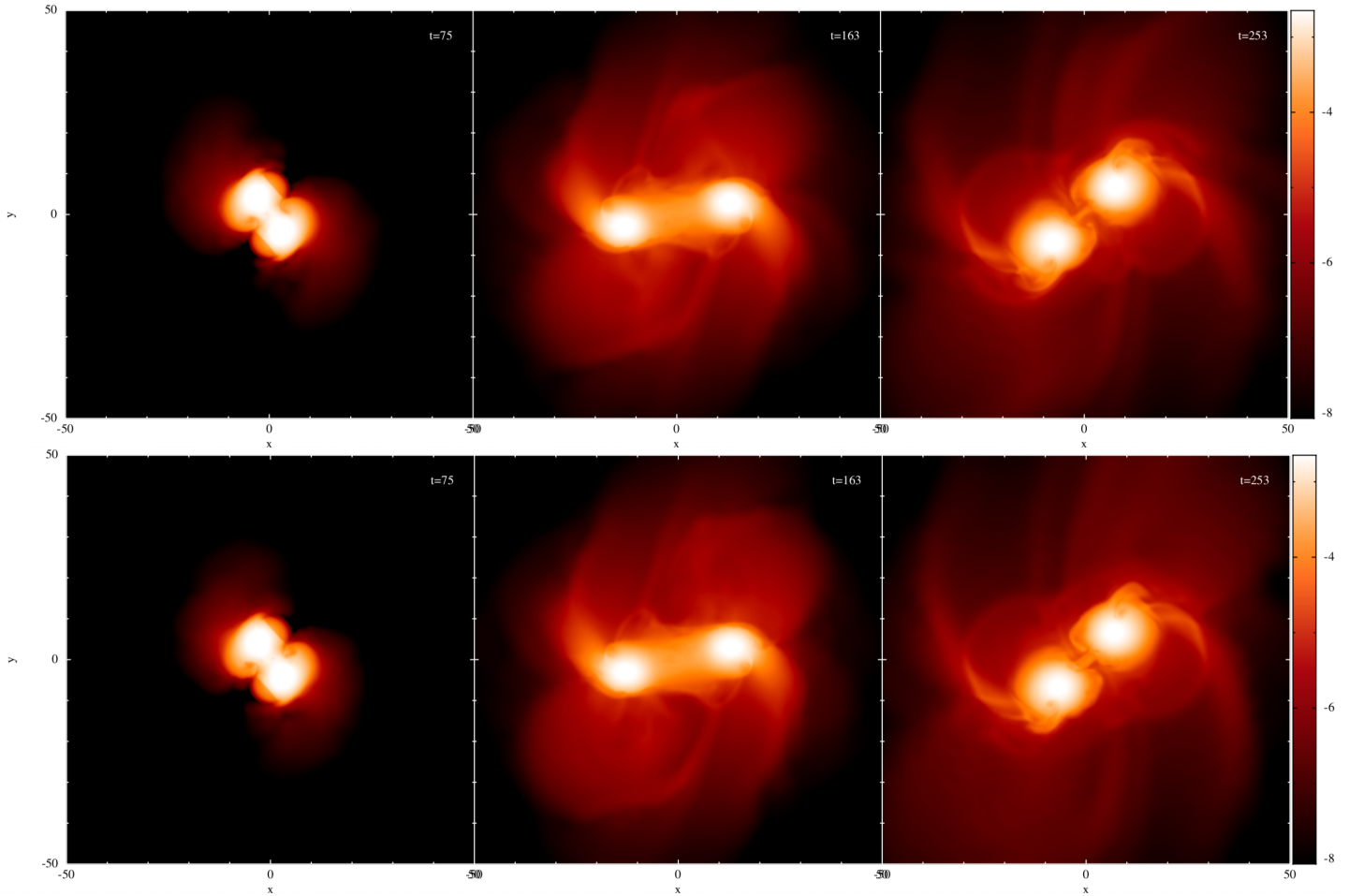


Figure 29. Off-center collision between two main sequence stars with an impact strength of $\beta = 3$, colour coded is density (in code units: 1989.1 g/cm^3 for density, time unit is 86.8 seconds). The upper row shows the results from a simulation that uses standard kernel gradients (stdGrad) in the evolution equation while the lower row shows the simulation that calculates gradients via a matrix-inversion technique (MI1). For this test both methods are in excellent agreement.

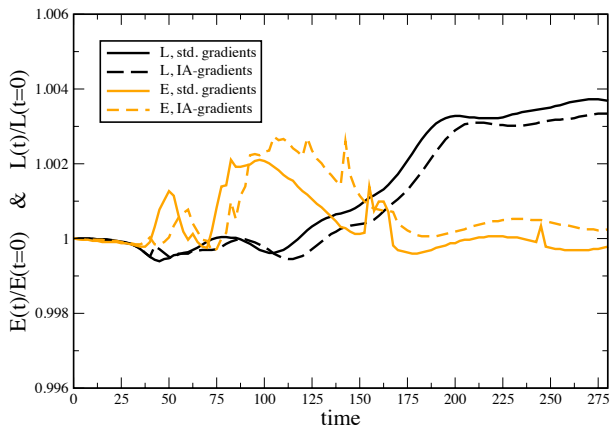


Figure 30. Conservation of total energy and angular momentum in the stellar collisions shown in Fig. 29. Both are shown for both simulations (with standard and IA-gradients) and are normalised to their initial values. Time is given in code units of 86.8 seconds.

robust against non-ideal particle setups. For example, in shock tests with particles placed on a cubic lattice it leads easier to particle "ringing effects". However, such problems can be easily cured by a more sophisticated particle setup such as via the above described APM.

We have further performed a number of the challenging, vorticity-creating shocks suggested by Schulz-Rinne (1993). Also here, MAGMA2 yields crisp results that are comparable with those from established Eulerian methods. We have also performed a number of more astrophysical simulations (stellar collision and tidal disruptions by black holes) to demonstrate the robustness of MAGMA2 and its accurate numerical conservation.

In none of the comparisons did we find any disadvantage of the matrix-inversion gradient prescription. But in many tests they showed clearly superior performance. Since the computationally expensive ingredients (long neighbour loops, matrix inversions, self-gravity) are shared by all three SPH formulations, we do not find substantial differences in their run times. As practically demonstrated in the stellar collision example, the matrix inversion formulations perform equally well in terms of numerical conservation as standard kernel gradients.

In its current version, MAGMA2 has implemented only self-

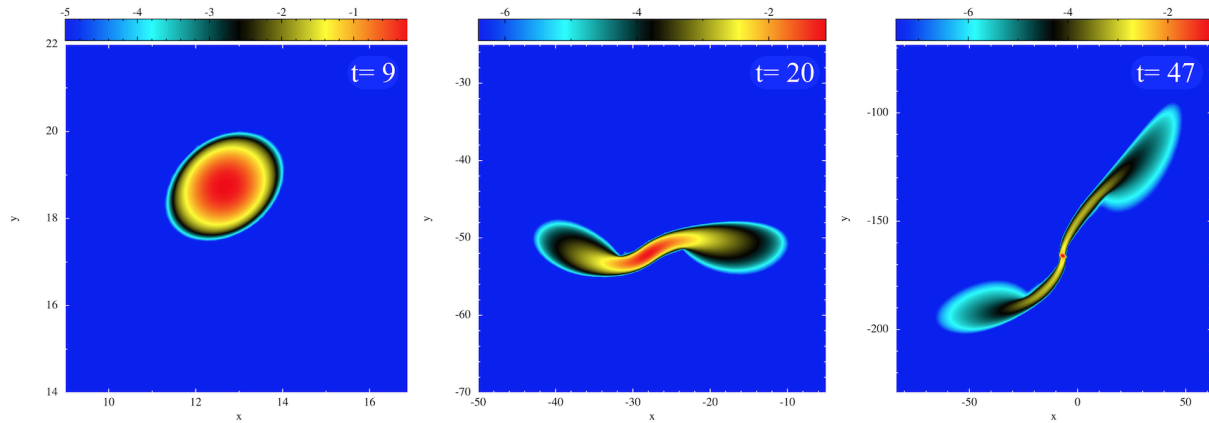


Figure 31. 3D tidal disruption of a $0.5 M_{\odot}$ white dwarf star (modelled with 5×10^6 SPH particles) by a $1000 M_{\odot}$ black hole located at the coordinate origin. This is a weak encounter (penetration factor $\beta = 0.9$) where the white dwarf actually passes outside the tidal radius and becomes “nearly disrupted”. After the passage, however, the core contracts again due to self-gravity. Colour-coded is the mass density in the orbital plane.

gravitating gas dynamics with polytropic equations of state, but this framework will be enriched in the near future by more physics.

ACKNOWLEDGEMENTS

It is a great pleasure to thank Ilya Mandel for sharing the initial conditions of the double-TDE and Stephen Justham for providing stellar profiles of the corresponding masses. Thank you also to Davide Gizzi and Christoffer Lundman for their careful reading of an earlier draft. Some of the figures of this article were produced with the visualization software SPLASH (Price & Monaghan 2007). This work has been supported by the Swedish Research Council (VR) under grant number 2016-03657_3, by the Swedish National Space Board under grant number Dnr. 107/16, by the research environment grant “Gravitational Radiation and Electromagnetic Astrophysical Transients (GREAT)” funded by the Swedish Research Council (VR) under Dnr 2016-06012 and by the Knut and Alice Wallenberg Foundation under Dnr. KAW 2019.0112. We gratefully acknowledge support from COST Action CA16104 “Gravitational waves, black holes and fundamental physics” (GWverse) and from COST Action CA16214 “The multi-messenger physics and astrophysics of neutron stars” (PHAROS). The simulations for this paper were performed on the facilities of the North-German Supercomputing Alliance (HLRN) in both Göttingen and Berlin, and on the SNIC resources Tetralith and Beskow.

REFERENCES

- Abel T., 2011, *MNRAS*, 413, 271
- Agertz O., Moore B., Stadel J., Potter D., Miniati F., Read J., Mayer L., Gawryszczak A., Kravtsov A., Nordlund Å., Pearce F., Quilis V., Rudd D., Springel V., Stone J., Tasker E., Teyssier R., Wadsley J., Walder R., 2007, *MNRAS*, 380, 963
- Ben Moussa B., Lanson N., Vila J., 1999, *International Series of Numerical Mathematics*, 29
- Benz W., Bowers R., Cameron A., Press W., 1990, *ApJ*, 348, 647
- Brandenburg A., Dobler W., 2002, *Computer Physics Communications*, 147, 471
- Cabezón R. M., García-Senz D., Escartin J. A., 2012, *A & A*, 545, A112
- Cabezón R. M., García-Senz D., Figueira J., 2017, *A & A*, 606, A78
- Cabezón R. M., García-Senz D., Relano A., 2008, *Journal of Computational Physics*, 227, 8523
- Casanova J., Jose J., García-Berro E., Shore S. N., Calder A. C., 2011, *Nature*, 478, 490
- Cha S.-H., Inutsuka S.-I., Nayakshin S., 2010, *MNRAS*, 403, 1165
- Cha S.-H., Whitworth A. P., 2003, *MNRAS*, 340, 73
- Chow J. E., Monaghan J., 1997, *J. Computat. Phys.*, 134, 296
- Christensen R. B., 1990, *Nuclear Explosives Code Developers Conference*, volume UCRL-JC-105269. Lawrence Livermore National Lab, Lawrence Livermore Technical Report., UCRL-JC-105269
- Cullen L., Dehnen W., 2010, *MNRAS*, 408, 669
- Dave R., Dubinski J., Hernquist L., 1997, *New Astronomy*, 2, 277
- Dehnen W., Aly H., 2012, *MNRAS*, 425, 1068
- Diehl S., Rockefeller G., Fryer C. L., Riethmiller D., Statler T. S., 2012, *ArXiv e-prints*
- Du Q., Faber V., Gunzburger M., 1999, *SIAM Review*, 41, 637
- Evrard A. E., 1988, *MNRAS*, 235, 911
- Frontiere N., Raskin C. D., Owen J. M., 2017, *Journal of Computational Physics*, 332, 160
- Gaburov E., Nitadori K., 2011, *MNRAS*, 414, 129
- Gafton E., Rosswog S., 2011, *MNRAS*, 418, 770
- García-Senz D., Cabezón R., Escartin J., 2012, *A & A*, 538, A9
- Giacomazzo B., Zrake J., Duffell P. C., MacFadyen A. I., Perna R., 2015, *ApJ*, 809, 39
- Gottlieb S., Shu C. W., 1998, *Mathematics of Computation*, 67, 73
- Hernquist L., 1993, *ApJ*, 404, 717
- Hernquist L., Katz N., 1989, *ApJS*, 70, 419
- Heß S., Springel V., 2010, *MNRAS*, 406, 2289
- Hietel D., Steiner K., Struckmeier J., 2000, *Mathematical Models and Methods in Applied Sciences*, 10, 1363
- Hopkins P. F., 2013, *MNRAS*, 428, 2840
- Hopkins P. F., 2015, *MNRAS*, 450, 53
- Hu C.-Y., Naab T., Walch S., Moster B. P., Oser L., 2014, *ArXiv e-prints*
- Hubber D. A., Rosotti G. P., Booth R. A., 2018, *MNRAS*, 473, 1603

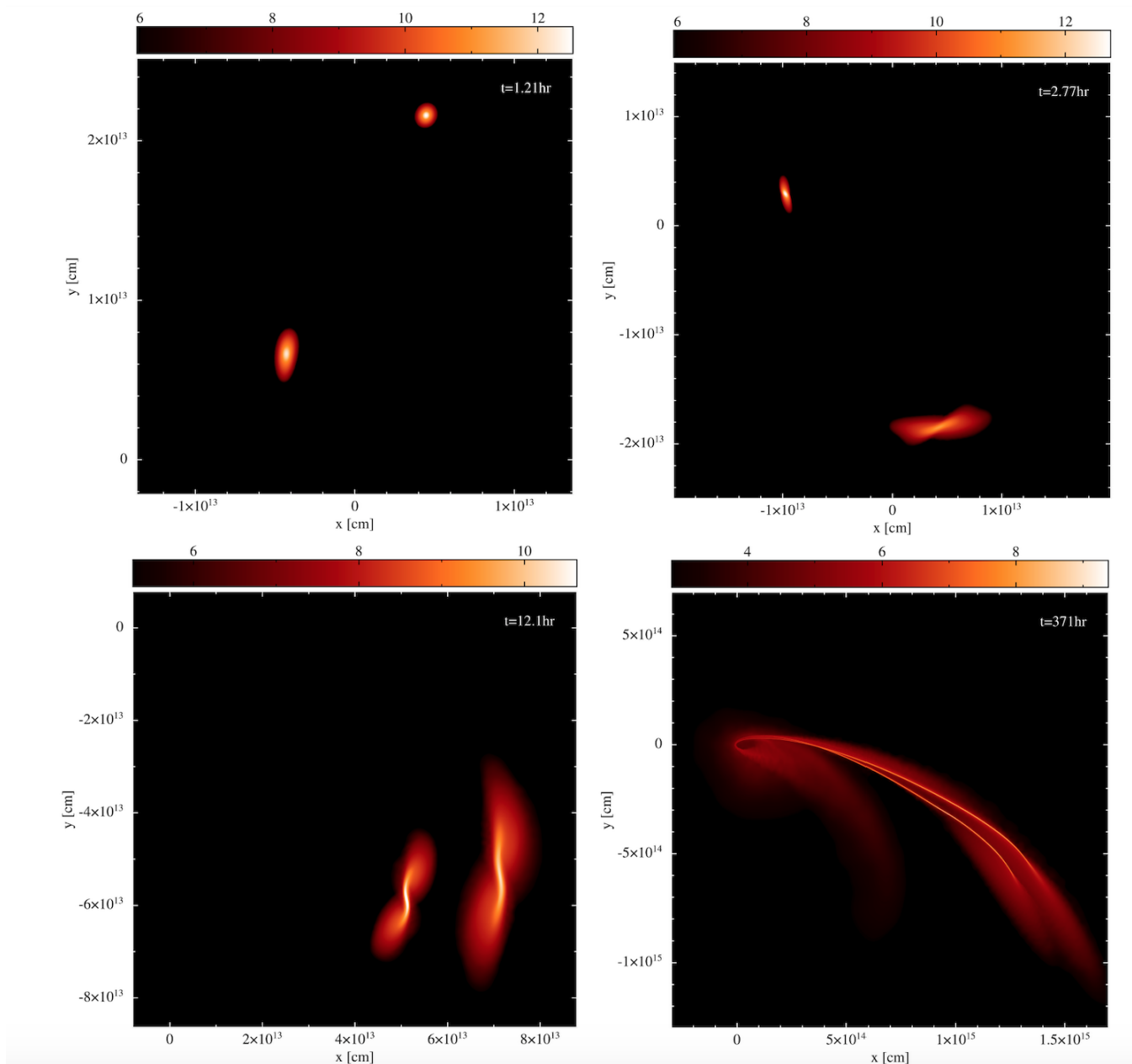


Figure 32. Tidal disruption of a binary system consisting of two massive stars (67.01 and $36.8 M_{\odot}$) by a supermassive black hole ($10^6 M_{\odot}$).

Inutsuka S.-I., 2002, *Journal of Computational Physics*, 179, 238
 Johnson J. R., Wing S., Delamere P. A., 2014, *Space Science Reviews*, 184, 1
 Junk M., 2003, In: Griebel M., Schweitzer M.A. (eds) *Mesh-free Methods for Partial Differential Equations. Lecture Notes in Computational Science and Engineering*, vol 26. Springer, Berlin, Heidelberg, 26, 223
 Kiuchi K., Cerdá-Durán P., Kyutoku K., Sekiguchi Y., Shibata M., 2015, *Phys. Rev. D*, 92, 124034
 Kurganov A., Tadmor E., 2002
 Lax P., Liu X., 1998, *SIAM J. Sci. Comput.*, 19, 319
 Liska R., Wendroff B., 2003, *SIAM J. Sci. Comput.*, 25, 995
 Liu W. K., Jun S., Zhang Y. F., 1995, *International Journal for Numerical Methods in Fluids*, 20, 1081

Lombardi J., Sills A., Rasio F., Shapiro S., 1999, *J. Comp. Phys.*, 152, 687
 Lucy L., 1977, *The Astronomical Journal*, 82, 1013
 Luminet J.-P., Pichon B., 1989, *A&A*, 209, 85
 Mandel I., Levin Y., 2015, *ApJL*, 805, L4
 McNally C. P., Lyra W., Passy J.-C., 2012, *ApJS*, 201, 18
 Monaghan J., 1977, *M.N.R.A.S.*, 181, 375
 Monaghan J., Gingold R., 1983, *J. Comp. Phys.*, 52, 374
 Monaghan J. J., 1992, *Ann. Rev. Astron. Astrophys.*, 30, 543
 Monaghan J. J., 1997, *Journal of Computational Physics*, 136, 298
 Monaghan J. J., 2002, *MNRAS*, 335, 843
 Monaghan J. J., 2005, *Reports on Progress in Physics*, 68, 1703
 Monaghan J. J., Price D. J., 2001, *MNRAS*, 328, 381
 Morris J., Monaghan J., 1997, *J. Comp. Phys.*, 136, 41

- Murante G., Borgani S., Brunino R., Cha S.-H., 2011, *MNRAS*, 417, 136
- Noh W. F., 1987, *Journal of Computational Physics*, 72, 78
- Press W. H., Flannery B. P., Teukolsky S. A., Vetterling W. T., 1992, *Numerical Recipes*. Cambridge University Press, New York
- Price D., 2004, PhD thesis, University of Cambridge, arXiv:astro-ph/0507472
- Price D., Monaghan J., 2007, *MNRAS*, 374, 1347
- Price D., Rosswog S., 2006, *Science*, 312, 719
- Price D. J., 2008, *Journal of Computational Physics*, 227, 10040
- Price D. J., 2012, *Journal of Computational Physics*, 231, 759
- Price D. J., Wurster J., Tricco T. S., Nixon C., Toupin S., Pettitt A., 2018, *Publications of the Astronomical Society of Australia*, 35, e031
- Puri K., Ramachandran P., 2014, *Journal of Computational Physics*, 270, 432
- Read J. I., Hayfield T., Agertz O., 2010, *MNRAS*, p. 767
- Ritchie B. W., Thomas P. A., 2001, *MNRAS*, 323, 743
- Rosswog S., 2009, *New Astronomy Reviews*, 53, 78
- Rosswog S., 2010a, *J. Comp. Phys.*, 229, 8591
- Rosswog S., 2010b, *Classical and Quantum Gravity*, 27, 114108
- Rosswog S., 2015a, *MNRAS*, 448, 3628
- Rosswog S., 2015b, *Living Reviews of Computational Astrophysics* (2015), 1
- Rosswog S., 2020, *ApJ*, 898, 60
- Rosswog S., Davies M. B., Thielemann F.-K., Piran T., 2000, *A&A*, 360, 171
- Rosswog S., Price D., 2007, *MNRAS*, 379, 915
- Rosswog S., Ramirez-Ruiz E., Hix R., 2008, *ApJ*, 679, 1385
- Rosswog S., Ramirez-Ruiz E., Hix R., 2009, *ApJ*, 695, 404
- Saitoh T. R., Makino J., 2009, *ApJL*, 697, L99
- Saitoh T. R., Makino J., 2013, *ApJ*, 768, 44
- Schoenberg I., 1946, *Quart. Appl. Math.*, 4, 45
- Schulz-Rinne C. W., 1993, *SIAM Journal of Mathematical Analysis*, 24, 76
- Schüssler I., Schmitt D., 1981, *A & A*, 97, 373
- Sedov L. I., 1959, *Similarity and Dimensional Methods in Mechanics*
- Sod G., 1978, *J. Comput. Phys.*, 43, 1
- Springel V., 2010a, *MNRAS*, 401, 791
- Springel V., 2010b, *ARAA*, 48, 391
- Springel V., Hernquist L., 2002, *MNRAS*, 333, 649
- Springel V., Yoshida N., White S. D. M., 2001, *New Astronomy*, 6, 79
- Steinmetz M., Müller E., 1993, *A & A*, 268, 391
- Taylor G., 1950, *Proceedings of the Royal Society of London Series A*, 201, 159
- Tejeda E., Gafton E., Rosswog S., Miller J. C., 2017, *MNRAS*, 469, 4483
- Tejeda E., Rosswog S., 2013, *MNRAS*, 433, 1930
- Toro E., 1999, *Riemann Solvers and Numerical Methods for Fluid Dynamics*. Springer, Berlin
- Tricco T. S., 2019, *MNRAS*, 488, 5210
- Valdarnini R., 2012, *A & A*, 546, A45
- van Leer B., 1974, *Journal of Computational Physics*, 14, 361
- Vila J., 1999, *Mathematical Models and Methods in Applied Science*, 02, 161
- von Neumann J., Richtmyer R. D., 1950, *Journal of Applied Physics*, 21, 232
- Wadsley J. W., Keller B. W., Quinn T. R., 2017, *MNRAS*, 471, 2357
- Wadsley J. W., Stadel J., Quinn T., 2004, *New Astronomy*, 9, 137
- Wendland H., 1995, *Advances in Computational Mathematics*, 4, 389